· Article · Advances in Polar Science
doi: 10.13679/j.advps.2018.0045 September 2019 Vol. 30 No. 3: 303-327

Late Maastrichtian–Paleocene chronostratigraphy from Seymour Island, James Ross Basin, Antarctic Peninsula: Eustatic controls on sedimentation

Manuel MONTES[1*], Elisabet BEAMUD[2], Francisco NOZAL[1] & Sergio SANTILLANA[3]

[1] Instituto Geológico y Minero de España (IGME), Área de Geología, Geomorfología y Cartografía Geológica, Calera 1, 28760-Tres Cantos, Madrid, Spain;
[2] Paleomagnetic Laboratory CCiTUB-Instituto de Ciencias de la Tierra 'Jaume Almera'-CSIC, Sole i Sabaris, s/n, 08028-Barcelona, Spain;
[3] Instituto Antártico Argentino, 25 de Mayo 1143, San Martín, provincia de Buenos Aires, Argentina

Received 5 December 2018; accepted 6 February 2019; published online 8 April 2019

Abstract The Paleocene (66–56 Ma) was a critical time interval for understanding the geological history in high palaeolatitudes after the end of Cretaceous event (recovery from mass extinction, palaeoclimate, global sea level changes, among others). The sedimentary succession from Seymour Island (Antarctic Peninsula) provides key reference material from this important phase of the early Cenozoic. A detailed age model is proposed for the López de Bertodano Formation (LBF), Sobral Formation (SF) and Cross Valley–Wiman Formation (CVWF) based on a new magnetostratigraphic section which integrates previous dinoflagellate cyst biostratigraphy, Iridium anomaly (K-Pg boundary), U-Pb zircon dating (airfall tuff) and strontium isotope values from macrofossils. The new composite magnetostratigraphic section, which includes the Cretaceous–Paleogene boundary, has been correlated to the GPTS from C29r up to C24r. The top of the LBF is confirmed as latest Maastrichtian to earliest Danian (~65.4 Ma) in age. The overlying SF is mostly Danian in age (~65.2– ~63 Ma) and CVWF is Selandian–Thatenian (~61.3–56.9 Ma). LBF, SF and CVWF are unconformity-bounded units (alloformations) that record the geological evolution of the James Ross Basin during a period of relative decreasing tectonism but coeval with volcanic activity. Unconformity based internal units have been recognized, dividing each formation into allomembers (LBF: Molluscan and Cenozoic; SF: A, B and C; CVWF: Díaz, Arañado, Bahía Pingüino). The new age model allows correlation of base-level changes with eustatic sea-level fluctuations. The bases of the SF and CVWF are correlated with the 65.3 and 61.5 Ma sea level lowstands.

Keywords **Paleocene, magnetostratigraphy, Antarctic Peninsula, James Ross Basin, Seymour Island**

Citation: Montes M, Beamud E, Nozal F, et al. Late Maastrichtian–Paleocene chronostratigraphy from Seymour Island, James Ross Basin, Antarctic Peninsula: Eustatic controls on sedimentation. Adv Polar Sci, 2019, 30(3): 303-327, doi: 10.13679/j.advps.2018.0045

1 Introduction

Sea-level fluctuations have a significant influence on stratal architecture of continental margins and interior basins. Eustacy also controls hydrographic-climatic patterns and, indirectly, biotic patterns as well. Differentiating between the effects of eustacy and tectonics in the sedimentary record has been a major goal of sedimentologists and stratigraphers. Although the chronology of fluctuating global sea levels is regarded as a key factor in the

* Corresponding author, ORCID: 0000-0003-1036-4580, E-mail: m.montes@igme.es

development of sequence stratigraphy, there is no consensus about the global synchrony of these changes. Furthermore, differentiating eustatic from tectonic events is contentious, even in passive margin settings. One aim of this paper is to present a case study from the Paleocene of the James Ross Basin, northern Antarctic Peninsula (Figure 1).

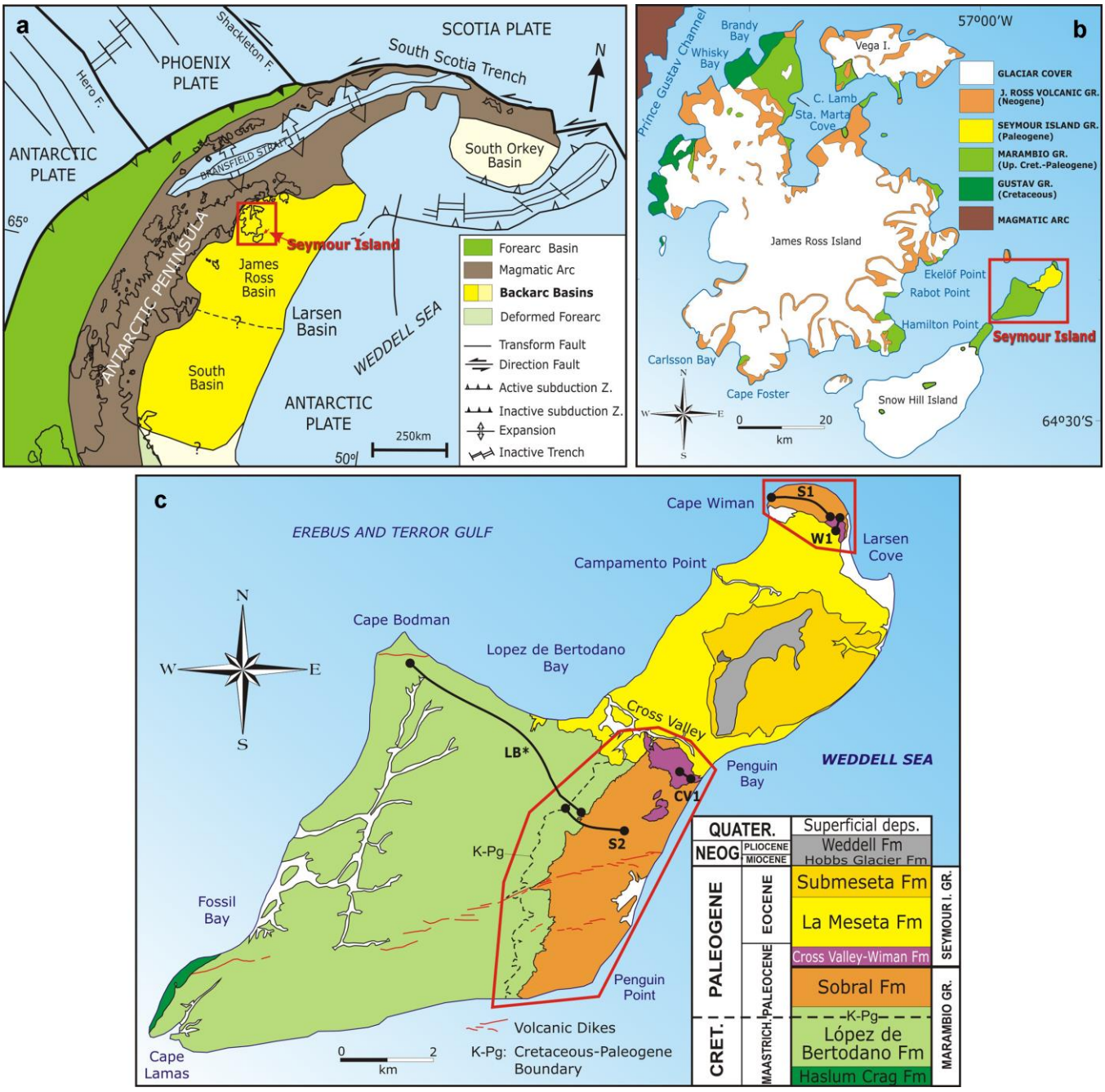

Figure 1 Geotectonic sketch map of the Antarctic Peninsula, after Marenssi et al. (2002) and Bohoyo (2004) (**a**). Location of the Seymour Island in James Ross Basin showing the distribution of Cretaceous and Cenozoic stratigraphic groups (**b**). Geology of Seymour Island, after Montes et al. (2013, 2019). The red line show the outcrops represented in Figure 2. LB* (Tobin et al., 2012), S1, W1, CV1 and S2 are the locations of magnetostratigraphic sections (**c**).

In addition, the Paleocene (66–56 Ma) was a time of relative cooler global climate between the greenhouse phases of the mid Cretaceous and Eocene (Zachos et al., 2001; Royer, 2006; Zachos et al., 2008). During the Paleocene, global biotas changed significantly in response to several major environmental perturbations. It is possible that a period of intense volcanic outgassing during the latest Maastrichtian to earliest Danian from the Indian Deccan Peninsula had global effects (Courtillot and Fluteau, 2010; Schoene et al., 2015). Furthermore, there was a major

meteorite impact at the Cretaceous–Paleogene (K-Pg) boundary coincident with mass extinctions of marine plankton and major changes in terrestrial vegetation (Schulte et al., 2010; Molina, 2015). There is a growing volume of evidences to suggest that some key components of the modern Southern Ocean marine fauna had their origins in the Early Cenozoic (Crame et al., 2014).

The only onshore exposure of strata of this age in the Antarctica is on ice-free Seymour Island, at ~64° South, in the James Ross Basin at the tip of the Antarctic Peninsula (Figure 1; Elliot et al., 1994; Montes et al., 2008a, 2008b, 2013, 2019; Bowman et al., 2012, 2014a, 2016). During the Cretaceous and Paleogene, sediments of the Marambio Group that now form much of the island were being deposited in mid shelf and deltaic settings in a back-arc basin at a similar palaeolatitude (Hathway, 2000; Crame et al., 2004; Olivero, 2012; Martos et al., 2014). The succession is highly fossiliferous, is suitable for magnetostratigraphical analysis (Tobin et al., 2012), and has several ash beds (airfall tuffs) preserved above the K-Pg boundary into the Sobral Formation (SF, Figures 2, 7 and 8). Previous work has refined the age of the oldest part of the Seymour Island succession (Haslum Crag and the López de Bertodano Formations) as Maastrichtian to earliest Danian using dinoflagellate cyst biostratigraphy correlated to magnetostratigraphy and strontium isotope stratigraphy (Askin, 1988a; McArthur et al., 1998; Olivero et al., 2008; Tobin et al., 2012; Bowman et al., 2012, 2014a). The focus of this paper is the study of new measured sections through the uppermost López de Bertodano Formation (LBF), across the K-Pg boundary, and through the overlying SF and Cross Valley–Wiman Formation (CVWF) in the SE and N part of the island (Figure 1). The LBF, SF and CVWF have a new high-resolution stratigraphy (allomembers and cartographic units) recently mapped at scale 1:20000 (Montes et al., 2013, 2019).

We also present a detailed age model for the succession, across the K-Pg boundary into the Paleocene in order to provide a robust chronostratigraphic framework for this reference outcrops. The emphasis is put on the magnetostratigraphic analysis of the mentioned sections which have been correlated to the Geomagnetic Polarity Timescale (Gradstein et al., 2012). The overall age model includes previous work on palynomorphs and other fossil groups (Macellari, 1986; Askin, 1988a, 1988b; Huber, 1988; Olivero and Medina, 2000; Bowman et al., 2012, 2016; Crame et al., 2014). Supporting evidence also includes previous magnetostratigraphic data (Tobin et al., 2012); U-Pb isotope dates from zircons extracted from airfall tuff horizons (Bowman et al., 2016); strontium isotope analyses from macrofossils (McArthur et al., 1998; Crame et al., 2004) and the Iridium anomaly at the K-Pg boundary (Elliot et al., 1994).

The precise age model for the Paleocene on Seymour Island allows a correlation with the eustatic sea level curves which helps to identify the sea level control on the sedimentation patterns.

2 Geological setting

The Larsen Basin (Figure 1a) is located on the continental shelf off the coast of the northern Antarctic Peninsula (Macdonald et al., 1988). The better-known James Ross Basin (del Valle et al., 1992) is the northern sub-basin of the Larsen Basin (Figure 1a). A 6–7 km-thick sedimentary succession was deposited between Jurassic and Eocene times in continental–marine environments related to the evolution of the Larsen Basin from a continental-rift to a back-arc setting (Hathway, 2000).

The sedimentary infill of the James Ross Basin has been divided into a series of megasequences separated by boundaries that record main periods of change in basin configuration. The youngest of these megasequences consists on an ?Aptian–Eocene aggradational–progradational deep-to shallow-marine clastic wedge, deposited along a faulted western margin of the Antarctic Peninsula during a phase of arc uplift and extension (Hathway, 2000).

Pirrie et al. (1991) suggested that marginal and intrabasinal tectonism in the James Ross Basin was on the decline after Coniacian times. Sedimentation was subsequently controlled by base-level changes, with a magnitude of 50–100 m (and probably less than 50 m), but the biostratigraphic resolution at that time prevented them from constraining whether these changes were tectonically or eustatically driven. The former can tentatively be recognized during the latest stages of basin development as tectonic activity declined.

Coniacian–Eocene sediments in the James Ross Basin reflect mainly shallow-marine and coastal environments (Macellari 1988; Pirrie et al., 1991; Marenssi et al., 1998a; Olivero, 2012). Basin uplift or decreased basin subsidence outpaced by sedimentation led to the development of a broad shallow shelf (Pirrie et al., 1991; Olivero, 2012) that was sporadically emergent during the Palaeogene (Sadler, 1988; Marenssi et al., 1998b). As a consequence of the development of this broad, stable shelf, decreased synsedimentary tectonic deformation and decreased coeval arc volcanism, sedimentation was most probably controlled by eustatic sea-level changes. The bedding tilt up to 10 degrees of the whole Marambio Group and the lower part of the Seymour Group could be explained by tectonic processes after the Paleocene–Eocene. However, some limits of stratigraphic formations consisting of large erosive surfaces (lower boundary of La Meseta Formation) may have been produced by the joint action of tectonism, still present in the basin, and eustatism.

3 Stratigraphic framework: Latest Maastrichtian–Paleocene from Seymour Island

The upper part of the sedimentary record of the James Ross Basin is located on Seymour Island and is included into the Marambio Group (Maastrichtian–lower Paleocene) and the

Seymour Island Group (upper Paleocene–upper Eocene) (Figure 1b). In addition, the upper Maastrichtian and Paleocene sediments are contained in the LBF, SF, and CVWF (Figure 1c)

3.1 López de Bertodano Formation (LBF)

The LBF (Rinaldi et al., 1978), occupies the SW of the island, between Cape Bodman and Cross Valley (Figure 1c). The LBF, comprises relatively homogeneous and unconsolidated marine clay-silts and silty-clays, with interbedded concretions, often following thin burrowed sand deposits (Macellari, 1988; Bowman et al., 2012; Olivero, 2012). It has been broadly interpreted as a transgressive shelf succession, much of the formation representing midshelf conditions above a basal estuarine unit (Macellari, 1988; Olivero et al., 2007, 2008; Olivero, 2012). The formation contains abundant fossils of marine invertebrates, fossil traces and, some levels, also contain fossil vertebrates and fossil wood remnants. The most complete profile is located on the southern coast line (Macellari, 1988) between Cape Lamas and Penguin Point, where the LBF exceeds 1300 m (Figure 1c).

The subdivision into members of the formation has been hampered by the high degree of homogeneity and the great facies similarity. Macellari (1988) divides the formation into ten cartographic units (Klb 1–10); and two informal units for his paleontological content: "Rotularia Units" (Klb 1–6), and "Molluscan Units" (Klb 7–10). Crame et al. (2004) include the first of these units (Klb 1) within the Snow Hill Formation, and subsequently Olivero et al. (2008), defines it as new formation: Haslum Crag Formation. The LBF, so understood, rests in a marked unconformity on the Haslum Crag Formation. In addition, Crame et al. (2004), suggest the possibility of treating as a member the intervening Cenozoic deposits (Klb 10) between the K-Pg and SF.

Finally, more recent works and the new Geological Map of Seymour Island (Montes et al., 2013, 2019), divide the LBF into three members: Rotularias Allomember (lower, 2–6 units); Molluscan Allomember (middle, 7–9 units) and Cenozoic Allomember (upper, 10–11 units). The latter is equivalent to the Cenozoic deposits of the LBF above the K-Pg boundary.

These lithostratigraphic schemes (Molluscan and Cenozoic Allomembers) have been correlated to a composite section in order to accurately relate previous biostratigraphy (Huber, 1988; Macellari, 1988; Olivero and Medina, 2000; Bowman, et al., 2012, 2016).

The increasing content of glaucony, typically concentrated in thin sandy fossiliferous units that form resistant ridges, characterize the uppermost part of the LBF. The top of unit 8 (8g) and 9 (9g) (K-Pg boundary) are an example of such units. Some petrological studies concluded that the glaucony was autochthonous in nature (Bowman et al., 2016). This suggests that, although the LBF represents an expanded Maastrichtian–earliest Paleocene section overall, deposition on the shelf was interrupted by periods of slow, condensed sedimentation, which have been interpreted as representing the base of parasequences (Olivero et al., 2017)

The K-Pg boundary on Seymour Island occurs within the upper LBF, where it is located near the base of a prominent composite glaucony-rich unit (Figures 2 and 3b), within what has been termed the "Lower Glauconite" (Elliot et al., 1994; Zinsmeister, 1998). The base of the unit is typically gradational (Elliot et al., 1994; Zinsmeister, 1998) though sharp, erosional contacts are observed in places. The boundary is positioned within the lower few metres of this unit on the basis of dinoflagellate cyst and macrofaunal biostratigraphy and an iridium anomaly (Askin, 1988b; Elliot et al., 1994; Zinsmeister, 1998; Bowman et al., 2012, 2013a; Witts et al., 2015). The uniformity of the bioturbated glauconitic muddy sands through this interval suggests that sedimentation was relatively continuous across the K-Pg boundary itself (see also Elliot et al., 1994) and suggested a period of slow, condensed sedimentation (Macellari, 1988; Olivero et al., 2017).

The Cenozoic Allomember (~100 m, 10–11 units of Montes et al., 2013, 2019) extends from the Weddell Sea in the S, towards the N until it is eroded under the basal unconformity of the Eocene sediments of the La Meseta Formation. Across and above the K-Pg boundary, the uppermost LBF is similar to the rest of the underlying formation, but is characterized by the drastic disappearance of most of the faunal groups of the Cretaceous (ammonites, molluscs, serpulids, echinoid spines, etc.). Unit 10 is equivalent to the Klb10 of Macellari (1988). Unit 11 (new) is distinguished by the drastic disappearance of the concretionary levels and the bivalve *Lahilia* sp. which are frequent in the previous unit. It consists of a monotonous series of gray and greenish-green shales with sporadic decimetric laminated sandstones. Towards the base (S2, Figure 2) and in the middle part of the unit, two levels of 1 m thick dark shales rich in glauconite are visible (Figure 3a).

3.2 Sobral Formation (SF)

The SF (Rinaldi et al., 1978), is present in the southern sector of the island between Penguin Bay and Penguin Point and in the northern area around Cape Wiman. Both sectors are separated by the outcrops of the La Meseta Formation (Eocene), that constitutes the filling of an incised valley of ~6 km wide (Figure 2).

In the southern sector (Figure 2), it is located above the LBF, through a marked erosive surface (Figures 2 and 3). To show the geometry of the surface, 13 sections were made (S1–S13, Figure 2), correlated taking as reference the glauconite layer (unit 9g) close to the K-Pg boundary. The variable thickness of the Cenozoic Allomember of the LBF

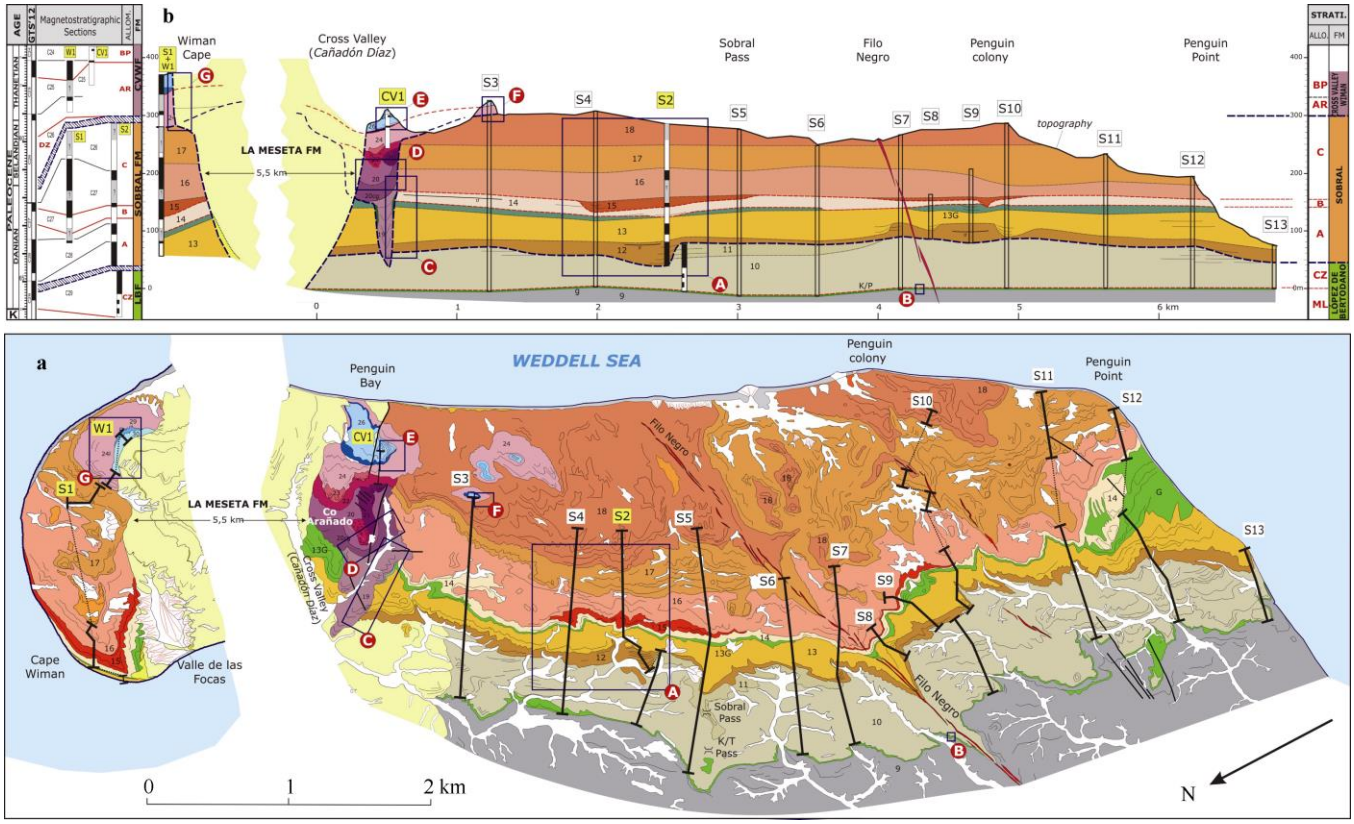

Figure 2 Geological sketch map of units (9–30) of late Maastrichtian–Paleocene of Seymour Island (after Montes et al., 2013, 2019): Molluscan (ML) and Cenozoic (CZ) allomembers of LBF, SF (A, B, C; allomembers) and CVWF (DZ: Díaz, AR: Arañado, BP: Bahía Pingüino; allomembers) (**a**). Correlation panel for SF (S1 to S13) and CVWF (CV1 and W1), showing the cartographic units geometry, and formation-allomembers discontinuities (erosion surfaces, unconformities, etc.). Labels in yellow represent the magnetostratigraphic sections. Left of panel: correlation with GTS'12 (Grandstein et al, 2012); see also text and Figure 8 for more details. The boxes and letters (A–F) represent the location of images in Figures 3 and 4 (**b**).

(units 10 and 11), gives an idea of the surface geometry. Sections S1 and S2 were sampled for magnetostratigraphy.

Classically, the SF has been divided into four cartographic units (TPs1–5, Sadler, 1988). Recent geological works and maps (Santillana et al., 2007; Montes et al., 2008a) divided SF into seven lithostratigraphic units (units 12–18), and three allomembers named: Sobral A, Sobral B and Sobral C, separated by internal discontinuities (erosive surfaces) (Figures 2 and 3). Each of the members, includes several cartographic units, whose equivalence is unequal with the units of Sadler (1988) (Figure 9).

In total, 250 m of thickness have been recorded for the SF, which maintains the same homoclinal structure (10º dip to the SE) with the previous formation, with which it forms the Marambio Group. The basal discontinuity does not appear in the Cape Wiman sector (Figure 2), but the three differentiated members are present.

The Sobral A Allomember (50–80 m; 12, 13 and 13G units) begins with centimetric rhythmites of shales and brownish fine-grained sands, with flaser-linsen structures and decametric erosive scars (12). The unit laps on the basal erosive surface of the SF. At the top of the unit (Figures 2 and 7) a yellowish level (0.5–1 m) of volcanic tuff (tf) crops out for a short distance. It has been dated by U-Pb geochronology on zircons at 65.05±0.15 Ma (Bowman et al., 2016). These deposits were interpreted as prodelta facies (Macellari, 1988). However, the sedimentary structures and their stratigraphic context would allow them to be interpreted as tidal rhythmites filling channels.

The upper unit (13), is represented by a residual deposit of accumulation of ostraea remains, corals and concretions with bivalves (Figures 3 and 7). Over this surface, brown laminated shales very bioturbated and concretions with abundant molluscan remnants, are present. The top of this section consists of three metric levels of greenish sands with concretions rich in autigenic glauconite (13G, Figure 3), and records a period of slow sedimentation, probably linked to a significant rise in relative sea level in a transgresive context (Macellari, 1988; Montes et al., 2008a).

The Sobral B Allomember (20 m; 14 unit) is placed in soft erosive unconformityon top of the Sobral A Allomember (Figure 3), totally eroding the previous glauconitic levels (S2 and S5, Figures 2 and 3). It consists

of an alternating series of brown laminated shales, fine gray sandstones and greenish sands with glauconite. In the northernmost sector, towards the top of the unit, a whitish level composed of volcanic ash (tf) is identified which testifies the existence of a contemporary volcanism with sedimentation.

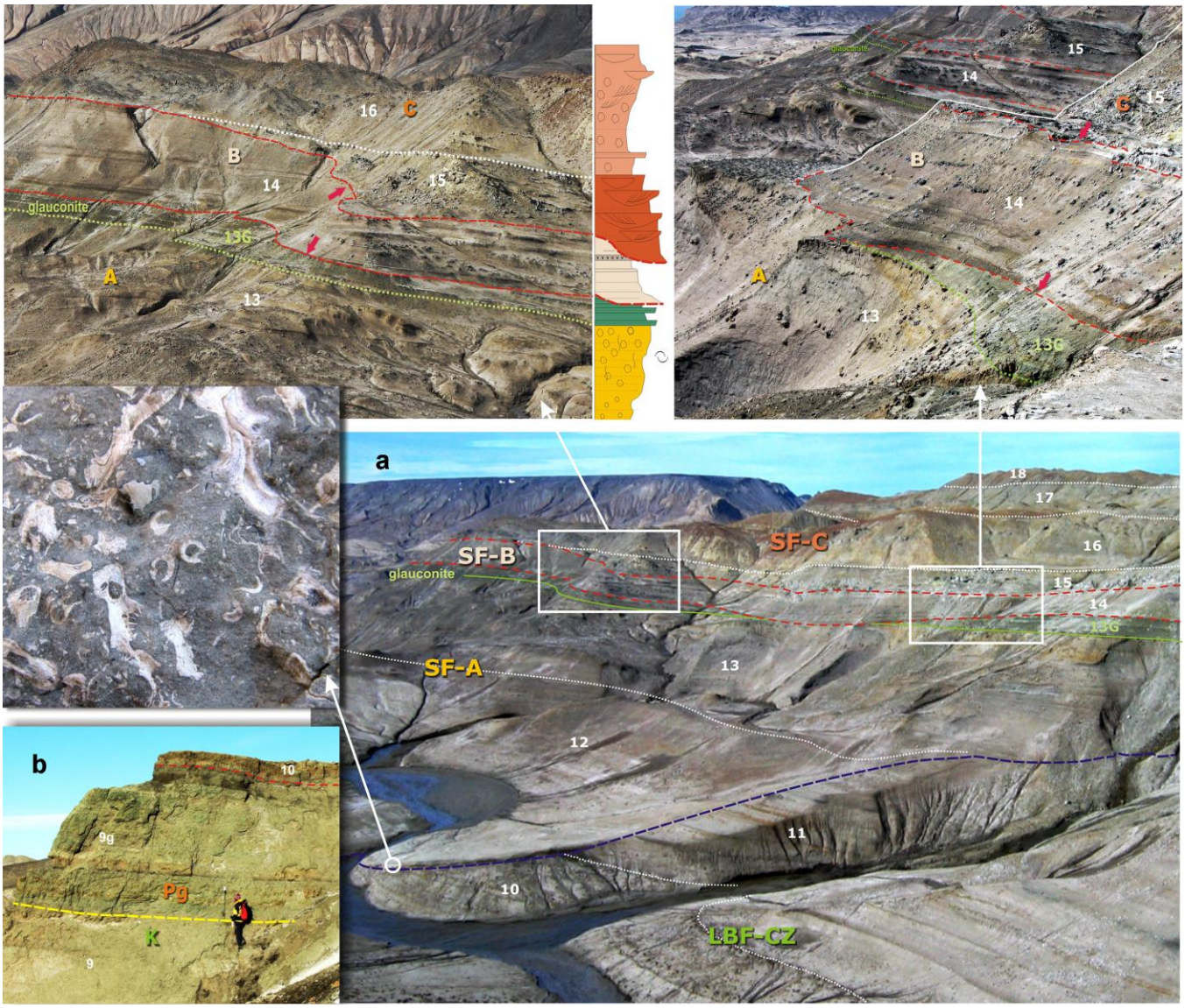

Figure 3 Overview of the SF (A in Figure 2, S2 section), showing lithological units and Sobral A, B and C, allomember, with their erosive basal surfaces. Great basal erosive discordance eroded to units 10 (with concretions levels) and 11 (without concretions and lutitic) of Cenozoic Allomember (LBF earliest Danian). The surface is covered by a coral breccia (detail). Left detail: internal erosive surfaces of SF and onlap infill geometries (arrows). Right detail: basal erosive surface of Sobral B Allomember eroding all glauconite rich beds (13G) at top of the Sobral A Allomember (**a**); Type section of K-Pg boundary in Seymour Island (B in Figure 2). Yellow line shows the position of the Iridium anomaly after Elliot et al. (1994). Glauconite (9g unit) is more abundant over Ir level (**b**).

The Sobral B Allomember is interpreted as external platform facies deposited in a transgressive context on top of an erosive surface produced as a consequence of a relative sea level lowering.

The base of the Sobral C Allomember (120–150 m; 15–18 units), is an erosive surface that eroded the previous unit (Figures 2 and 3), generating small incised channels that are filled by the basal unit of the allomember (15). It consists in an alternation of trough and tabular cross-bedding sandstones, with fine sandstones and laminated shales, forming thickening and fining upward sequences. These facies constitute the infill of erosive palaeochannels, probably tidally influenced, excavated during a relative descent of sea level.

The other three units are composed of laminated sandstones and sandstones with nodules and sandstone in palaeochannels to the top (16); sandstones with cross-bedding stratification with well-selected and

rounded green clasts of detrital glauconite (17); and thickening upward levels of sandstones with planar high angle cross-bedding stratification rich in bivalves (*Pinna* sp., 18).

The Sobral C Allomember would therefore represent a composite cycle with a first regressive stage with erosion and filling with tidal facies (15), a second transgressive stage (16) and finally, a regressive and progradational siliciclastic marine platform (16, 17 and 18).

3.3 Cross Valley–Wiman Formation (CVWF)

This new name (Montes et al., 2008b) includes the sediments of the Cross Valley Formation (Elliot and Trautman, 1982) outcropping in the narrowest area of the island, (Cross Valley, Figure 2); and Cape Wiman (N) deposits, called the Wiman Formation (Elliot and Hoffman, 1989).

For its stratigraphic characterization, five partial sections have been made in Cross Valley which have been synthesized in a composite section (CV1), and a section in the Wiman zone (W1). Both sections were sampled for magnetostratigraphy, although in CV1 only its upper part could be sampled.

In the outcrops of Cross Valley, the formation has been divided into five lithofacies (TPcv1–5, Sadler, 1988). Recent geological works and maps (Montes et al., 2008b) identify 11 lithostratigraphic units in the CVWF (19–30 by Montes et al., 2013, 2019) and two internal discontinuities (erosive surfaces), that divide the CVWF into three allomembers named: Díaz, Arañado and Bahía Pingüino (Figures 2 and 4).

The fact that the lower allomembers (Díaz and Arañado), contain significant amounts of volcanic components in lenticular bodies, which are wedged towards the margins of the channel, is noteworthy. Each allomember includes several of the mapped lithostratigraphic units, which have an unequal equivalence with those defined by Sadler (1988) (Figure 9).

The lithological characteristics and sedimentary facies of the deposits of the Cape Wiman area, led to the identification of three cartographic units (24l, 29 and 30), correlated with part of the Arañado Allomember (medium) and the Bahía Pingüino Allomember (upper), defined in the Cross Valley zone. These observations justify the inclusion of both outcrops in the new CVWF formation (Montes et al., 2008b).

In both outcrops, the base of CVWF, is a strongly erosive surface over the sediments of SF, with a very clear incised valley geometry (Figures 2 and 4a), with asymmetric slopes (45° toward N; 35° toward S) width of 600 m and length of about 1.5 km (Figure 2). The whole succession is inclined about 10° towards SE. The maximum observed incision is around 200 m, eroding on the sediments of the Sobral A Allomember (Figure 2), although erosion on the upper materials of the LBF is also possible.

As a whole, ~240 m thickness was recorded for the CVWF, which maintains the same homoclinal structure (10º dip to the SE) with the previous SF.

The Díaz Allomember (~120 m; 19g, 19, 20cg, 20 and 21 units) are the basal sediments that filled the incised valley, where three fining-upward sequences with palaeochannel geometry are identified. The lower sequence consists of coarse sands, sandstones and fine conglomerates at the base (19), with cross lamination and great content of volcanic (andesitic) and intraclast components and frequent remains of burned fossil wood. In outcrop, the colors are yellowish and orange. The grain size of the sediments gradually decreases upwards. These deposits lap on the edges of the palaeochannel (Figure 4b). In this lower part, the erosive surface of the CVWF, is covered by 1–5 m of greenish sandstones very rich in glauconite (19g, Figure 4b).

The middle sequence begins with greenish fine conglomeratic and sands entirely composed of volcanic rocks clasts (20cg, Figure 4c). They present a diffuse lamination, and towards the upper part they change to orange sands with burned fossil wood remnants, similar to the ones observed in unit 19.

Finally, the upper sequence has an erosive base with channel morphology, with greenish coarse and fine conglomeratic sandstones deposits (21).

The base of the Arañado Allomember (~70 m; 22br, 22, 23, 24 and 24l) is a marked erosive surface with channel geometry. Over this surface there are breccias and massive conglomerates, which form the relief of Arañado Hill (22br, Figure 4c). These thick detritic deposits quickly pass, both vertically and laterally, to well-selected sandstone facies (22), with trough and planar cross-bedding and fossil plant remains (23). This filling stage culminates with sandstones and shales, orange in color, with fossil wood (24, Figure 4d, 4e, 4f). It is important to note that this unit (24), is also the base of the small isolated outcrops in form of '*mesas*' (tables) south of the main ones (Figure 4f), frequently considered the top of the SF (TPs5 by Sadler, 1988; last 30 m SF from Bowman et al., 2016). As this unit clearly belongs to Arañado Allomember we interpret these outcrops within the CVWF.

This facies would represent the culmination of the filling of the deepest part of the incised valley. The lower part of the three units, which are observed in the outcrops at Cape Wiman (unit 24l), with facies similar to 24, would belong to the Arañado Allomember.

The Bahía Pingüino Allomember (25–50 m; 25, 26, 27, 28, 29 and 30) represents a significant change in the filling, as the clastic composition is mostly siliciclastic. These deposits form small hills of flat summit ('*mesas*') towards the top of the formation (Figure 4d). The lower limit is a smooth erosive surface with channel morphology. Two sequences are recognized: a lower term of dark marls with oysters, fish teeth, sharks vertebral disks, echinoids, gastropods and penguins bones (25, 27); and an upper term

of sandstones and silty gray siltstones with plant debris (26, 28) (Figure 4d).

These facies are interpreted as lagoons or calm waters protected bays and represent the culmination of the general regressive filling observed for the formation. The upper part of the Cape Wiman outcrops with siliciclastic sandstones and fine conglomerates, would belong to this unit (29, 30; Figure 4e).

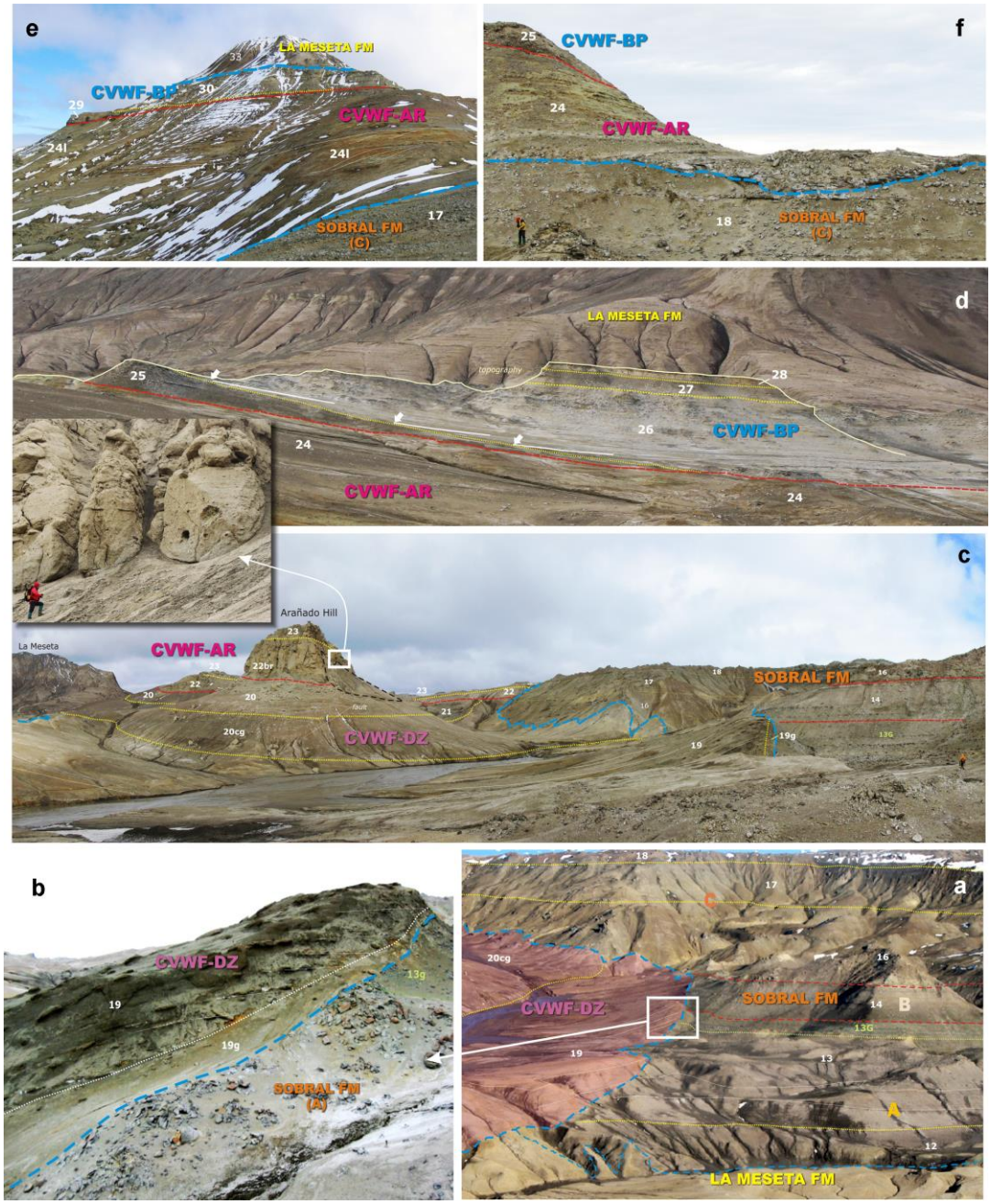

Figure 4 Helicopter overview (Cross Valley zone) showing the southern edge of the incised valley (C in Figure 2). It is observed how all members of the SF are cut (**a**). Onlapping geometry detail of unit 19 beds. Unit 19g (glauconite rich), cover the erosional surface (**b**); Geometry of the filling of lower CVWF, showing the beds onlap at both edges of the incised valley (D in Figure 2). Detail of volcanoclastic breccias (22br) in Arañado Hill (**c**). Cartographic units of Penguin Bay Allomember overview toward NE (E in Figure 2). The base of unit 26 erodes softly to 25 overlapping on 24 (Arañado Allomember). Beds of unit 26 onlapping over the erosive surface (white arrows). This palaeochannel is oriented towards NE, almost perpendicular respect to main one (towards the SE) (**d**). CVWF in Cape Wiman outcrops (G in Figure 2), showing cross-bedding lamination of unit 24l (volcanoclastic). Unit 29 are siliciclastic microconglomerates filling a palaeochannel (**e**). Top of S3 section (F in Figure 2), erroneously attributed by Sadler (1988) and Bowman et al. (2016), as top of SF (TPs5). Actually, the marked erosive surface over SF, is overlaid by unit 24 belonging to Arañado Allomember of CVWF. The erosive surface would cover the deposit time hiatus of Díaz and Arañado (part) Allomembers (**f**).

In general, the deposits of the different units of the CVWF are interpreted as the detrital filling of a marine incised valley on the preceding siliciclastic platform. This strong erosive discontinuity over the Marambio Group homoclinal (LBF and SF) and the resulting sedimentary change, were the arguments to consider it as the basal discordance of the Seymour Group (Elliot and Trautman, 1982).

4 Magnetostratigraphy

The magnetostratigraphic dating of the Paleocene series of Seymour Island builds on the new established stratigraphic framework. It is essential to obtain a robust age model and to constrain the relationships between sedimentation and sea level changes in the James Ross Basin. Four parallel magnetostratigraphic sections have been studied in two areas with Paleocene rocks outcrops (Figure 2).

4.1 The sampled sections

The magnetostratigraphic sections on Seymour Island extend over the LBF, SF and CVWF. In Cape Wiman sector (Figure 2) sections S1 and W1 have been studied (Figure 7). The samples on the S1 section were taken on the cartographic units of SF in the Sobral A, B and C allomembers (13 to 17 units) consisting mainly of silts, sandy silts, sands and fine to coarse sandstones. The samples in section W1 were taken on the cartographic units of the CVWF in the Arañado and Bahía Pingüino allomembers (24l, 29 and 30), consisting in un-consolidated sands and sandstones with volcanic clasts, intense lamination and remains of fossil wood; and laminated conglomerates and sandstones of siliciclastic composition.

Sections S2 and CV1 (Figure 7) are located in the SE sector of the island (Figure 2). Samples on section S2 were obtained from the LBF cartographic units (units 10 and 11, Cenozoic Allomember) and SF (units 12 to 18; Sobral A, B and C allomembers). They mainly consist of silty clays, silts, sandy silts, sands and fine to medium sandstones with some levels rich in glauconite. In section CV1, samples were taken from the cartographic units of the CVWF (24 to 28 units); Arañado and Bahía Pingüino allomembers). The coarse and poorly consolidated detrital sediments of the Díaz Allomember prevented sampling in this section.

Overall, 228 paleomagnetic sites were sampled spanning about 580 m in a composite stratigraphic section. In the Cape Wiman area, 117 sites were drilled along a composite stratigraphic succession (S1 and W1) 340 m thick. In the SE sector, 116 sites were taken along a composite section (S2 and CV1) of 366 m. Paleomagnetic sampling was a big issue due to outcrop conditions and the presence of permafrost in some of the intervals to be sampled. Therefore, a sampling strategy combining several extraction methods was adopted (Figure 5). First, outcrops were cleaned by digging ~ 50 cm deep in order to get access to unaltered rocks (Figure 5d). Whenever possible samples were drilled with an electrical cordless drill with diamond core bits cooled by water (Figure 5a). This was especially feasible when fine grained sandstone concretions were present within the stratigraphic succession. When sediments were too loose and soft to be drilled samples were obtained by means of insertion of standard paleomagnetic boxes (Figure 5b) and/or a soft sediments extractor pushed by a rubber hammer (Figure 5c). Whatever the type of the sampling method selected, samples were oriented in situ by means of a magnetic compass fixed to an orienting device with clinometer. All samples, except the ones in the paleomagnetic boxes, were consolidated with Na silicate and wrapped in foil in order to prevent deformation and vanishing of the samples during transport (Figure 5e). Sample position was marked with a GPS and placed within the stratigraphic sections, which were measured with a Jacob's staff. An average spacing of 2–3 m between sites was kept in all the magnetostratigraphic sections.

4.2 Paleomagnetic analysis

Paleomagnetic analyses were conducted at the Paleomagnetic Laboratory of Barcelona (CCiTUB–ICTJA CSIC). They consisted on stepwise demagnetization, thermal and/or by alternating field, and subsequent measurement of the Natural Remanent Magnetization (NRM) after every demagnetization step. The NRM was measured in a superconducting rock magnetometer (model 755R, 2G Enterprises) after demagnetization with thermal demagnetizers TSD1 (Schönstedt) and MMTD80 (Magnetic Measurements) or AF demagnetizer DTech2000 (ASC Scientific). Increments between 100 to 20℃ up to around 500℃ were applied for thermal treatment and AF fields ranging from 2 up to 140 mT were progressively applied during AF demagnetization (Figure 6). Characteristic components (ChRM) directions were obtained by principal component analyses (Kirschvink, 1980) after visual inspection of the demagnetization diagrams (Paldir software). Mean directions were obtained with the Pmag10 software developed by Lisa Tauxe. Additionally, rock magnetic experiments (IRM acquisition and 3 axes IRM demagnetization (Lowrie, 1990), were also conducted in order to identify the remanence carrier mineralogy (Figure A1 in supplementary material). IRM was applied with an impulse magnetizer IM10-30 (ASC Scientific) with coils up to 1.2 T.

In general, samples revealed low unblocking temperatures (around 300–400℃) and/or coercivities (30–60 mT) and showed an unstable behavior at relatively low temperatures or alternating fields (Figure 6; Table 1 in supplementary material). This behavior together with the

Figure 5 Photographies showing the sampling strategy: Electrical cordless drill cooled by water and orienting device (**a**); Standard paleomagnetic box (8cc) with orientation (**b**); Sampling with the soft sediments extractor (**c**); Outcrop cleaning (**d**); Consolidation of the samples with Na silicate solution (**e**).

IRM curves (Figure A1, supplementary material) point to a mixture of low coercivity (titano) magnetites of different grain size as the main remanence carriers. Most of the samples showed a low temperature component which was usually removed below 200℃ or 10 mT and which is interpreted as a recent overprint that will not be further considered. Characteristic components were classified as quality 1 or 2 when they were defined by at least 3 demagnetization steps and/or they were directed towards the origin. Conversely, when they could only be defined by 2 demagnetization steps and/or they showed scattered trajectories they were classified as class 3. Class 3 directions are represented with a different symbol (white square in Figure 7) and they are usually discarded to define the magnetozones in the local magnetostratigraphy (Figure 7). The low bedding dips (around 10° in all the sections) hindered the application of a fold test to check the primary character of the magnetization. It can be observed in Figure 6, that directions are very scattered and do not pass a reversal test. Moreover, the calculated directions show in general lower inclinations than expected for their latitudinal position. This scatter and the low inclinations may obey to the difficulty in cleaning and isolating the characteristic components from recent overprints due to the unstable behavior of most of the samples at low temperatures. Additionally, some post-depositional

deformation caused by bioturbation and/or the permafrost cannot be discarded. In general, the sections showed a very low success in isolation of the characteristic components. S1 yielded only a 10%–20% of successfully isolated directions, 25% of success was obtained for section W, 60% for section S2 and almost 90% in section CV. Consistent normal and reversed polarities were computed to obtain the virtual geomagnetic poles (VGPs) used to build the local magnetostratigraphy (Figure 7). This information is summarized in Table 1 of the supplementary material. Although the local magneto- stratigraphic sections present some uncertain intervals (represented in grey in Figure 7) it is worth pointing out that they pass the consistency test, as the polarity reversals are laterally traceable between distant sections and confirm the lithostratigraphic correlations.

The local magnetostratigraphy can be correlated to the GPTS (Granstein et al., 2012) through consideration of the new geological map and the available age constraints (Figure 8).

4.3 Previous age data

The Cretaceous units of LBF refer to the Maastrichtian on the basis of their ammonite fauna (Macellari, 1988; Olivero and Medina, 2000) and their intermediate stratigraphic position between the K-Pg boundary (Elliot et al., 1994) and Haslum Crag Formation, which contains the last levels with *Gunnarites antarcticus* of the lower Maastrichtian (Olivero et al., 2008; Olivero, 2012). Other available biostratigraphic data such as: foraminifera (Huber, 1988); palynomorphs (Askin, 1988; Zones 2–4); dinoflagellate cyst (Bowman et al., 2012); and rotularias (Macellari, 1988), confirm this Maastrichtian age. In addition, strontium isotope ($^{87}Sr/^{86}Sr$) values from molluscan, ~200 m below the K-Pg, support a Maastrichtian age (McArthur et al., 1998; Crame et al., 2004; Figure 10). Tobin et al. (2012) identified the chrons C31r (part), C31n, C30r, C30n, C29r and C29n (part) in their sections, which confirm an upper Maastrichtian age for these units. The lower part of our section S2 correlates well with two of the magnetozones above the K-Pg boundary shown by Tobin et al. (2012).

The Cenozoic Allomember of the LBF (units 10 and 11), is Danian in age for its concordant stratigraphic position on the K-Pg boundary (66.04 Ma), whose absolute dating, corresponds to the Iridium anomaly level

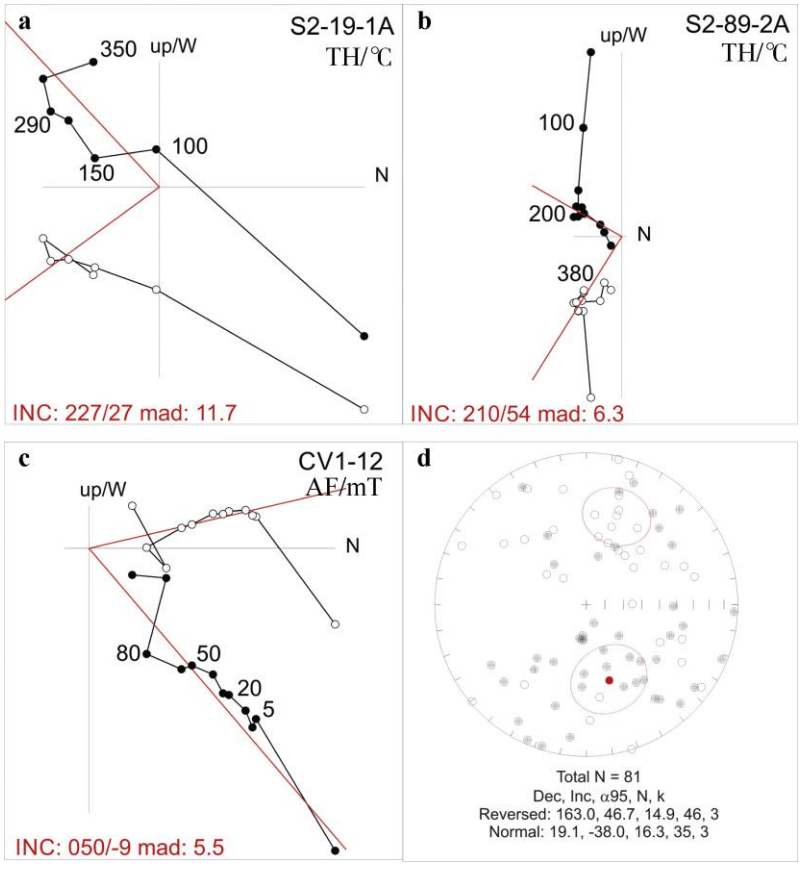

Figure 6 Demagnetization diagrams of selected samples (**a**, **b**, **c**) and individual characteristic components with mean directions (**d**). All diagrams are represented after tectonic correction. TH refers to thermal demagnetization and AF corresponds to alternating field demagnetization. **a** and **b** stand for reversed polarity samples of the SF. **c** stands for a normal polarity sample of the CVWF. Red lines in the demagnetization diagrams represent the calculated characteristic component.

studied by Elliot et al. (1994). In these units, the base of palynomorphs biozone 'Zone 5' (Askin, 1988) has been established; and also NZDP1-NZPD2 and *Hystrichosphaeridium tubiferum- Trithyrodinium evittii*, dinoflagellate cyst biozones (Bowman et al., 2016), belonging to the lower Danian. Strontium isotope ($^{87}Sr/^{86}Sr$) values from bivalves and gastropods from unit 10 (21 m and 71 m above K-Pg boundary in section studied by Bowman et al. [2016]; ~S3 in Figure 2) support a Danian age (McArthur et al., 1998).

The age of SF is Danian on the basis of content in palynomorphs (Zone 5, Askin, 1988); dinoflagellate cyst (NZDP3-NZDP4; *Palaeocystodinium golzowense-Palaeoperidium pyrophorum*; Bowman et al., 2016); and planktonic foraminifera (Zone D; Huber, 1988) obtained at the lower part of the formation (unit 12). In addition, Bowman et al. (2016), reports U-Pb isotope dates from zircons, extracted from airfall tuff horizons to top of unit 12 (level tf), at 65.05±0.15 Ma in age.

The CVWF would correspond to the upper Paleocene based on its stratigraphic position on top of Danian materials. On the other hand, the deposits of unit 24l (Cape Wiman) and 24 in the outcrops shaped 'tables' south of Cross Valley (TPs5 by Sadler, 1988), belonging to Arañado Allomember (top) and Bahía Pingüino Allomember, have an association of palynomorphs (Zone 6, Askin, 1988) and microfossils (Harwood, 1988; Wrenn and Hart, 1988) that indicate a Thanetian age. In addition, Bowman et al. (2016) in the same units (TPs5 by Sadler, 1988), identifies the biozones of dinoflagellate cyst NZDP7-8 and *Aspectodinium homophorphum*, of the upper Thanetian.

4.4 Correlation with the time scale

The local magnetozones of sections S1, S2, W1 and CV1 can be correlated to the GPTS'12, based on the previous chronological constraints and the lithostratigraphic correlations.

Section S2 includes the boundary K-Pg (66.04 Ma) and encompasses the last two units of LBF. Two magnetozones are identified, which can be unambiguously correlated to chrons C29r and C29n. This correlation is supported by the nearby studied section LB (Tobin et al., 2012). The stratigraphic position of the successive magnetozones in sections S1 and S2 as well as an absolute age of airfall tuff (65.05±0.15 Ma; top C29n) and dinoflagellate cyst biostratigraphy of Danian age, support correlation of the SF to C29n, C28r, C28n, C27r, C27n and C26r (part) (Figure 9). The SF erosive base, would be included into chron C29n.

Sections W1 and CV1 yielded interesting magneto-stratigraphic results despite their low resolution (Figure 7). The joint correlation of both sections shows the presence of three magnetozones of reverse polarity and two of normal polarity (Figures 7, 8 and 9), which can be correlated to chrons C26r, C26n, C25r C25n and C24r (top Selandian–Thanetian), compatible with dinoflagellate cyst biozones (Zone 6, Askin, 1988; NZDP7-8, Bowman et al., 2016), of Thanetian age. The Selandian, absent in the bio- and magnetostratigraphic data, would correspond to Díaz Allomember deposits. This would also explain the absence of NZDP5-6 dinoflagellate cyst biozones (Selandian) in the work of Bowman et al. (2016). The erosive base of CVWF would be included in the lower part of chron C26r.

4.5 Chronostratigraphy of late Maastrichtian–Paleocene of the James Ross Basin

The correlation of the sections with the GPTS (Gradstein et al., 2012, Figure 8) together with the previous chronostratigraphic data (chemo- and bio-), have been included in the composite section of LBF, SF and CVWF (Figure 9). Stratigraphic units have also been included with the equivalence with previous units (Macellari, 1988; Sadler, 1988) and correlated to the Geological Time Scale (GTS'12, Gradstein et al., 2012).

This correlation provides a robust age model for the late Maastrichtian-Paleocene stratigraphic units on Seymour Island and James Ross Basin (Figure 10).

5 Global sea-level chart and unconformities

From the sedimentological analysis of the different marine facies of the James Ross basin Maastrichtian–Paleocene deposits, several sedimentary environments can be inferred as originated by changes in relative sea level. Hence, the large erosive surfaces are interpreted as drastic sea level drops and consequent forced regressions and, the different relations between the sedimentary facies, as transgressive or regressive sequences (Macellari, 1988; Crame et al., 2004; Olivero et al., 2008; Montes et al., 2019).

When the chronostratigraphic framework obtained is confronted with the most recent eustatic curves (Kominz et al., 2008; GTS'12), it is evidenced that the erosive surfaces (expressed as the lower discontinuities of formations and allomembers), correspond to important hiatuses which agree with decreases in the eustatic curves. Also, there is a good correlation between transgressive and regressive sequences and maximum flooding surfaces associated with glauconite in the siliclastic platforms (Figure 9).

5.1 LBF: Maastrichtian–lowest Danian

Unit 7 at the base of the Molluscan Allomember ('Molluscan Units' of Macellari, 1988) contains a great variety of molluscan fauna with respect to previous units. This fauna enrichment and its sedimentological characteristics, allow interpreting this unit as deposited in an external and calm platform (Macellari, 1988; Crame

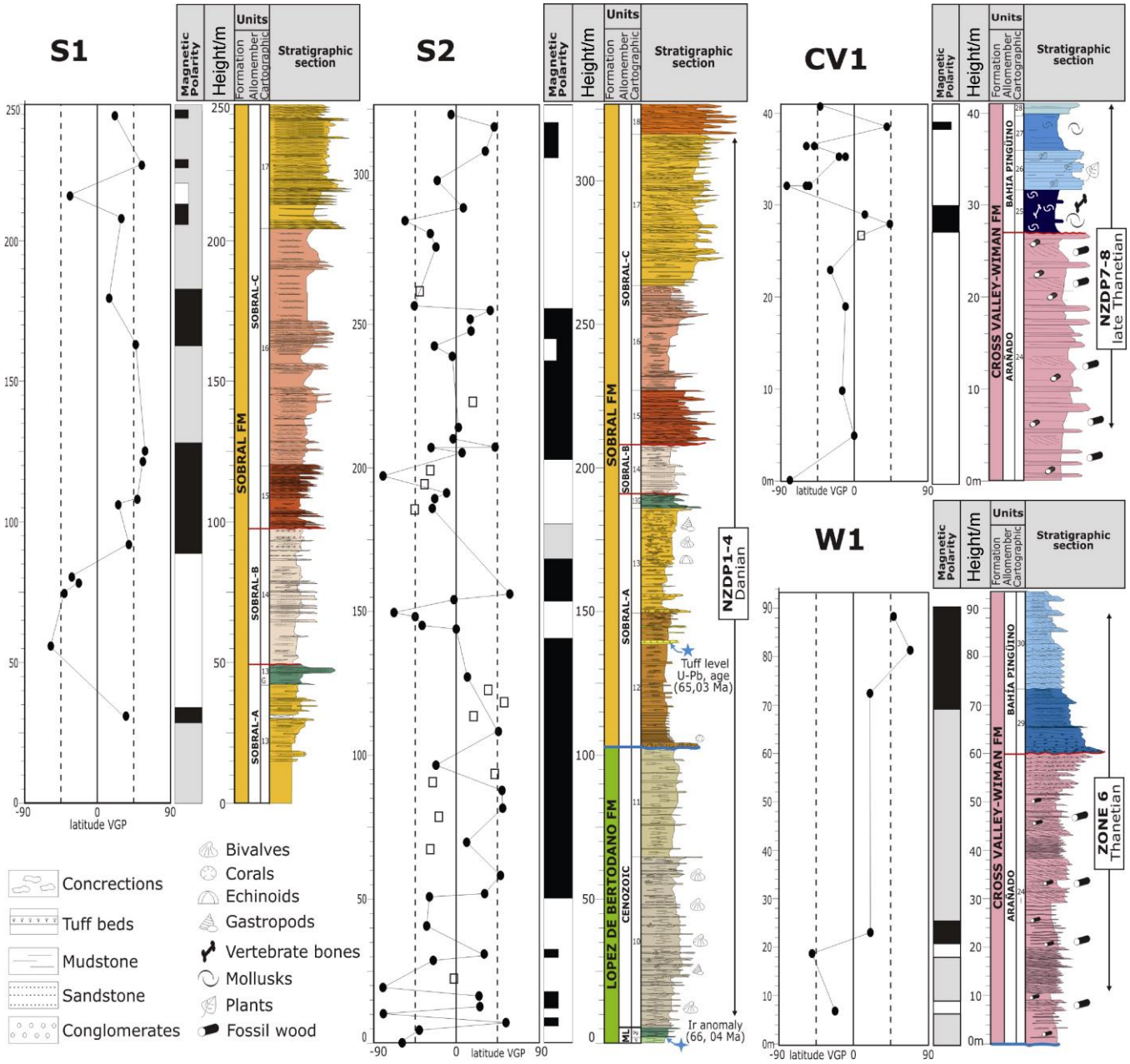

Figure 7 **S1** (Sobral-1) section contains stratigraphic units for SF in Cape Wiman. **S2** (Sobral-2) compiled units of upper half of LBF and SF, representing the top Maastrichtian and Danian interval. **W1** (Wiman) section compiled units of CVWF at Cape Wiman outcrops and representing the Paleocene top. **CV1** (Cross Valley) section contains results for the upper half of CVWF representing the top Paleocene. All sections contain a compiled litho-, bio- and magnetostratigraphic results. Lithostratigraphic units have been described by Montes et al. (2013, 2019). Dinoflagellate cyst and palynomorphs biostratigraphy by Askin (1988) (Zones 6) and Bowman et al. (2016) (NZDP1-8). Iridium anomaly has been described by Elliot et al. (1994). Airfall tuff U-Pb age, by Bowman et al. (2016). At left is the magnetic polarity interpretation, indicated by the Virtual Geomagnetic Pole after computing the paleomagnetic directions obtained. Black dots represent quality 1 and 2 samples, white squares represent quality 3 samples, which are not considered as reliable. The black bands represent normal polarity magnetozones; the white bands represent reversed polarity magnetozones and the grey bands indicate uncertain polarities.

et al., 2004). This interpretation is consistent with the dramatic rise in eustatic curve (Kominz et al., 2008) started ~70 Ma.

Units 8 and 9 would maintain the same facies, with more levels of sandstones and more glauconite content. Glauconite is a common autochthonous mineral in the

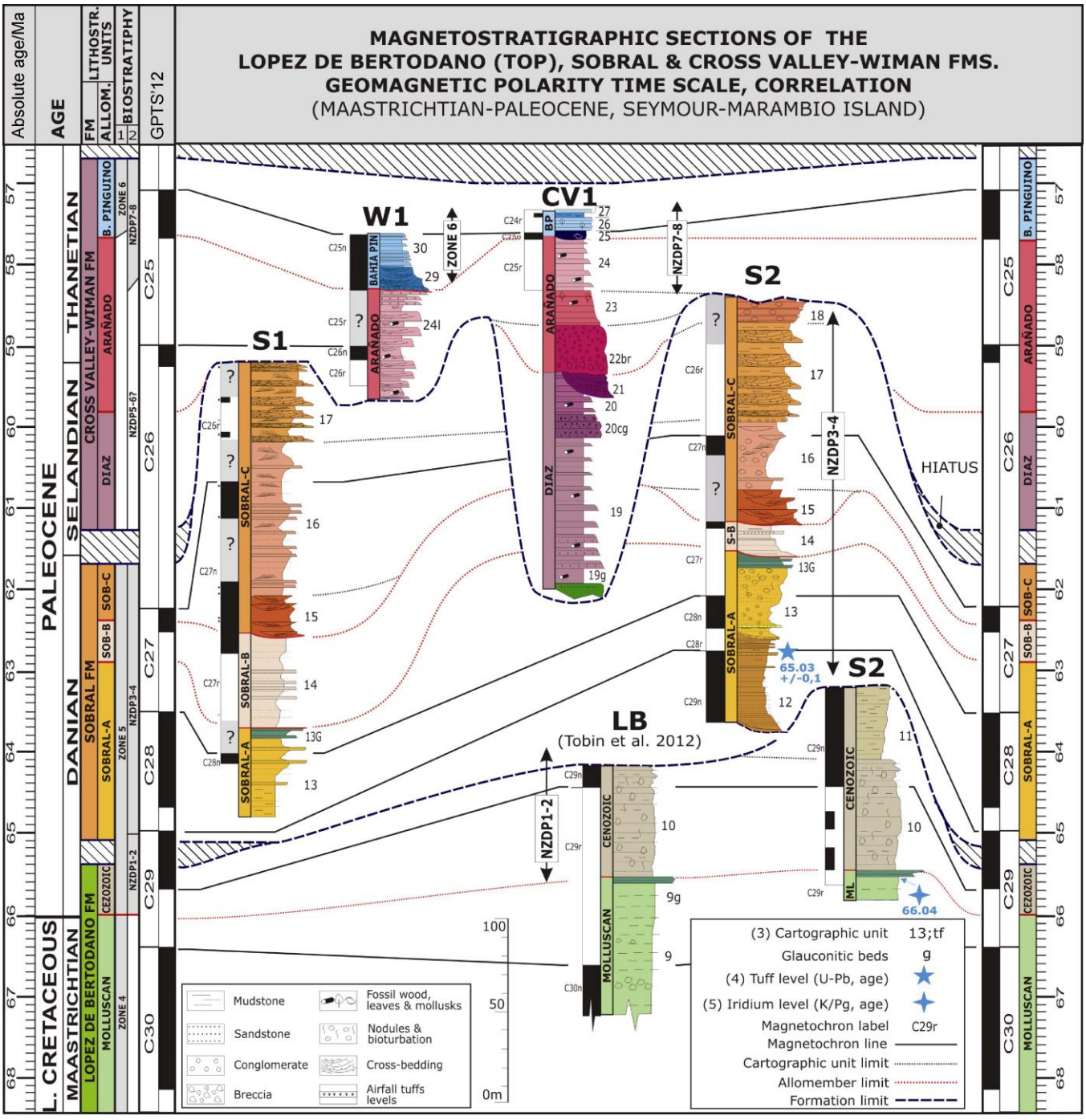

Figure 8 Lithostratigraphic studied sections and correlation of the local magnetostratigraphy to the GPTS'12 (Gradstein et al., 2012). Section LB after Tobin et al. (2012). References: dinoflagellate cyst and palynomorphs biostratigraphy: (1) Askin (1988) and (2) Bowman et al. (2016); lithostratigraphy: (3) Montes et al. (2013, 2019); absolute ages: (4) Bowman et al. (2016) and (5) Elliot et al. (1994).

offshore areas of siliciclastic platforms, frequently associated with the widespread condensed sections related to maximum flooding surfaces. They often merge landward associated with the widespread condensed sections related to maximum flooding surfaces. They often merge landward with transgressive surfaces. Glauconites are associated with slow sedimentation rates and they frequently occur in conjunction with organic matter (Odin, 1988; Harris and Whitin, 2000). GTS'12 curve for these units is maintained at same level with a general downward trend in Kominz curve, although in both there are some sharp declines. One of them coincides with the base of unit 8 (C31n, Tobin et al., 2012), culminated with level 8g glauconite rich (numerous plesiosaurs and mosasaurs are found there, Martin and

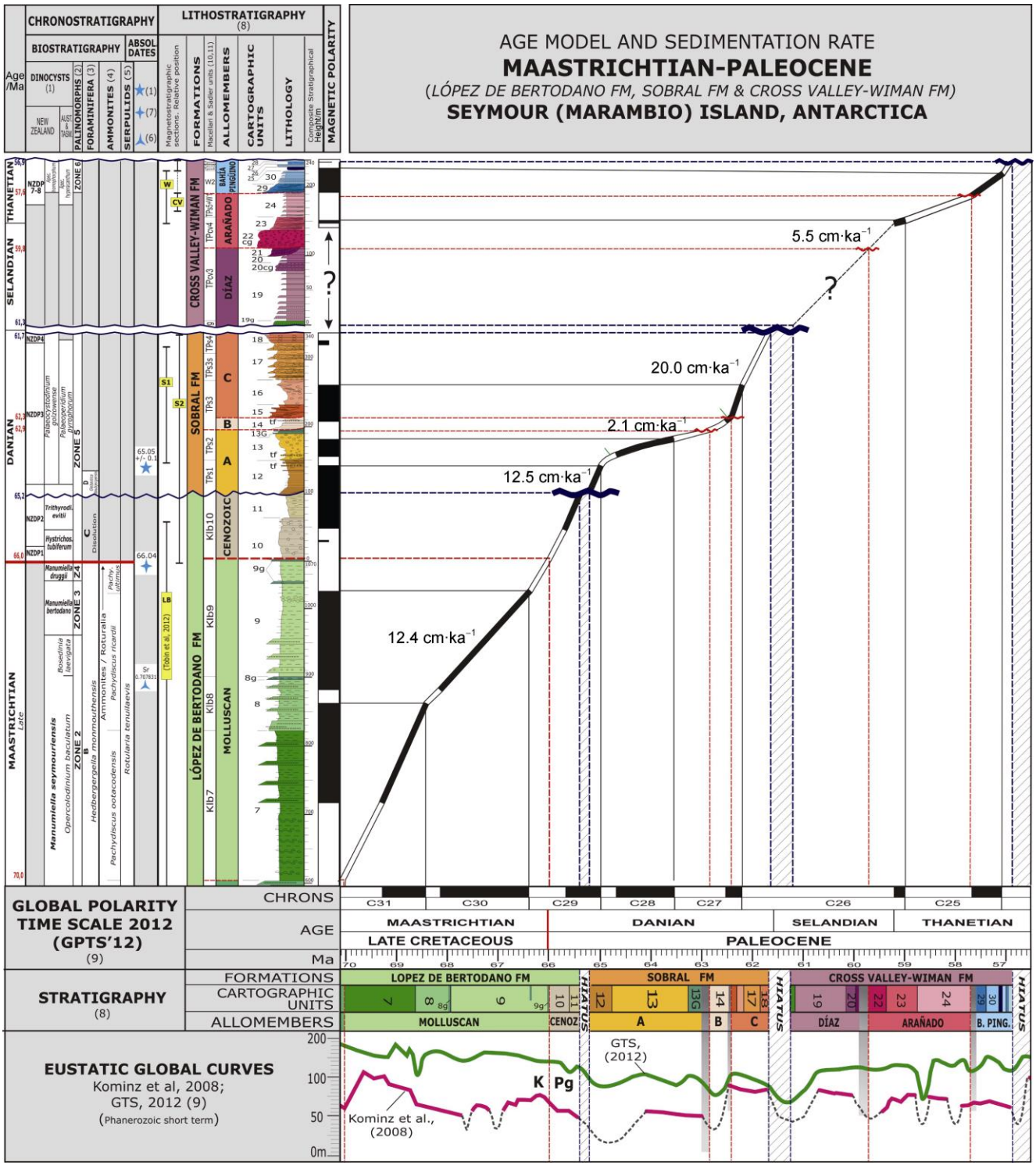

Figure 9 Local polarity scale correlation to the Geomagnetic Polarity Time Scale (GPTS'12). The available chronostratigraphic data of the LBF, SF and CVWF are shown to the left of the compiled section. Continuous black lines correlate the magnetozones of the local magnetostratigraphy with the GPTS'12. Blue lines bound the alloformation bases. Red lines bound the allomembers bases. The curve represents accumulation rate, with values in different stretches (cm·ka^{-1}). Biostratigraphic data and absolutes ages (K-Pg Ir anomaly and airfall tuff age), confirm the local magnetozones correlation with GPTS'12. The age of the cartographic units is obtained by interpolation. When comparing the age model with the most recent eustatic curves (Kominz et al. 2008; GTS'12), the graph shows that most of the erosive surfaces (alloformation, and allomembers boundaries) correspond to hiatuses related with sea level drops. References: (1) Bowman et al. (2016); (2) Askin (1988); (3) Huber (1988); (4) Olivero and Medina (2000); (5) Macellari (1988); (6) Crame et al. (2004); (7) Elliot et al. (1994); (8) Montes et al. (2013, 2019); (9) Grandstein et al. (2012); (10) Macellari (1988); (11) Sadler (1988).

Fernández, 2007; O'Keefe et al., 2017). This level would indicate a low sedimentation rate consistent with the maximum flooding surface derived from eustatic rise in GTS'12 curve. The base of unit 9 incorporates coarse detritic levels coherent with a progradation from the platform with sea level rise. Towards the top of this unit, glauconite levels reappear, to culminate with the K-Pg boundary, in a context compatible with rise of eustatic curves (Figures 9 and 10).

Cenozoic Allomember (10 and 11 units) show an increase in grain size and a greater presence of fossil wood suggesting a less deep sedimentary environment (Macellari, 1988), coinciding with a downward trend of the eustatic curve (Figures 9 and 10). The sedimentation rate of LBF (without decompacting) is 12.4 cm·ka^{-1} (Figure 9).

Paleoenvironmental studies (Bowman et al., 2014a) detect three peaks of abundance of the dinoflagellate *Impletosphaeridium clavus* in LBF. The upper one is located at the base of unit 8 (68.7 Ma). This taxon is typical of cold marine waters and could suggest episodes of cooling with temporary stratification of shallow marine waters, with some ice in the sea, alternating with smoother periods when waters are mixed. This could trigger glacier formation in higher levels in the Antarctic continent already in Cretaceous times, and also local or even global glacio-eustatic phenomena.

Over the last cold episode marked by *I. clavus*, several paleoclimate works based on isotopic studies (Tobin et al., 2012) and analysis of palynomorphs (Bowman et al., 2014a, 2014b), observed a significant warming of waters in the upper part of LBF and up to the K-Pg boundary. This warming is related to extinctions of unit 9 faunas before the K-Pg and, in turn, would be simultaneous with different phases of mass volcanism of India's Deccan Traps (Tobin et al., 2012).

5.2 Sobral Formation: Danian

The basal discontinuity of SF is interpreted as an erosive surface originated on a siliciclastic marine platform during a regressive period, due to a drastic drop in the relative sea level (Santillana et al., 2007; Marenssi et al., 2012; Montes et al., 2019). The sinuous geometry of its surface (Figure 2) suggests that the bottom was eroded by a series of palaeochannels perpendicular to the coastline.

This relative sea level drop is consistent with that occurring between 65 and 66 Ma in both eustatic curves (inside C29n). In outcrops, the observed erosion of 30–40 m is consistent with the amplitude of descent ~30 m according to the eustatic curve (Figures 9 and 10).

Sobral A Allomember (12) basal deposits have been interpreted as prodelta facies (Macellari, 1988). However, the sedimentary structures and their stratigraphic context allow them to be interpreted as rhythmites filling tidal channels in an estuarine environment. The accommodation space provided by eustatic descent is filled at a sedimentation rate of 12.5 cm·ka^{-1} (Figure 9). This calm water environment would favor the conservation of airfall tuff at the top of the unit, of 65.03±0.1 Ma (Bowman et al., 2016) (Figure 3).

The erosive base of next unit (13) represents a new episode of relative sea level drop. The presence of nodules with shelf mollusk fauna (gastropods, echinoids, corals, etc.) indicates a deeper sedimentary environment in a transgressive context. This context is consistent with rise in eustatic curves. However, the relative descent of sea level that could be deduced from the erosive surface at the base, does not coincide with any event in the eustatic curve (Figures 9 and 10). Changes in basin subsidence would be the explanation. In this sense, the presence of tuff levels (tf) in units 12 and 13 (S1, Figure 7), and the increase in volcanic clastic sandstones (Macellari, 1988; Hoffman, 1991; Marenssi et al, 2012) suggest a contemporary volcanism with uplift in the Antarctic Peninsula and an increase of subsidence in the platform.

Glauconitic levels at top of unit (13G) are interpreted as maximum flooding surface with low sedimentation rate within the same transgressive context (Odin, 1988; Amorosi, 1995; Harris and Whitin, 2000). This coincides with the highest level of the curve in this section (chron C27r, ~63.2 Ma; Figure 10) and decrease in sedimentary rate slope (2.1 cm·ka^{-1}, Figure 9).

The base of Sobral B Allomember, is a small erosive surface, 10–15 m of magnitude, but appreciable at outcrop scale (Figures 2 and 3). The whole allomember is interpreted as external platform facies deposited in a transgressive context on an erosive surface produced by a relative lowering of sea level. This decrease is correlated with descent of eustatic curves at ~62.9 Ma.

The base of Sobral C Allomember is an erosional surface incised about 25 m on the previous unit (Figures 2 and 3). It is also interpreted as produced by a relative sea level drop. Eustatic curves for this section are stable. However, the beginning of a soft descent is registered during chron C27n (~62.5 Ma), coherent with an erosive surface between units 14 and 15 (base of Sobral C Allomember). The magnitudes of eustatic descent are coherent for both erosive surfaces (Figures 9 and 10).

Unit 15 onlaps the erosive surface at the base of Sobral C Allomember. It is interpreted as the infilling of a palaeochannel with tidal influence. The overlying units (16, 17, 18), have been interpreted as prodelta, delta front and delta plain facies, with sediment supply towards the SE in a regressive context (Macellari, 1988). However, the absence of typical deltaic facies (lobes, channeled facies, etc.) and the continuity and extension of facies, provide a more plausible interpretation as deposits of a progradational siliciclastic marine platform. Sobral C Allomember, would therefore represent a composed cycle with a first regressive stage with erosion and filling of tidal channel facies (15), a second transgressive stage (16) and finally, a regressive sequence formed by the siliciclastic platform units (17–18).

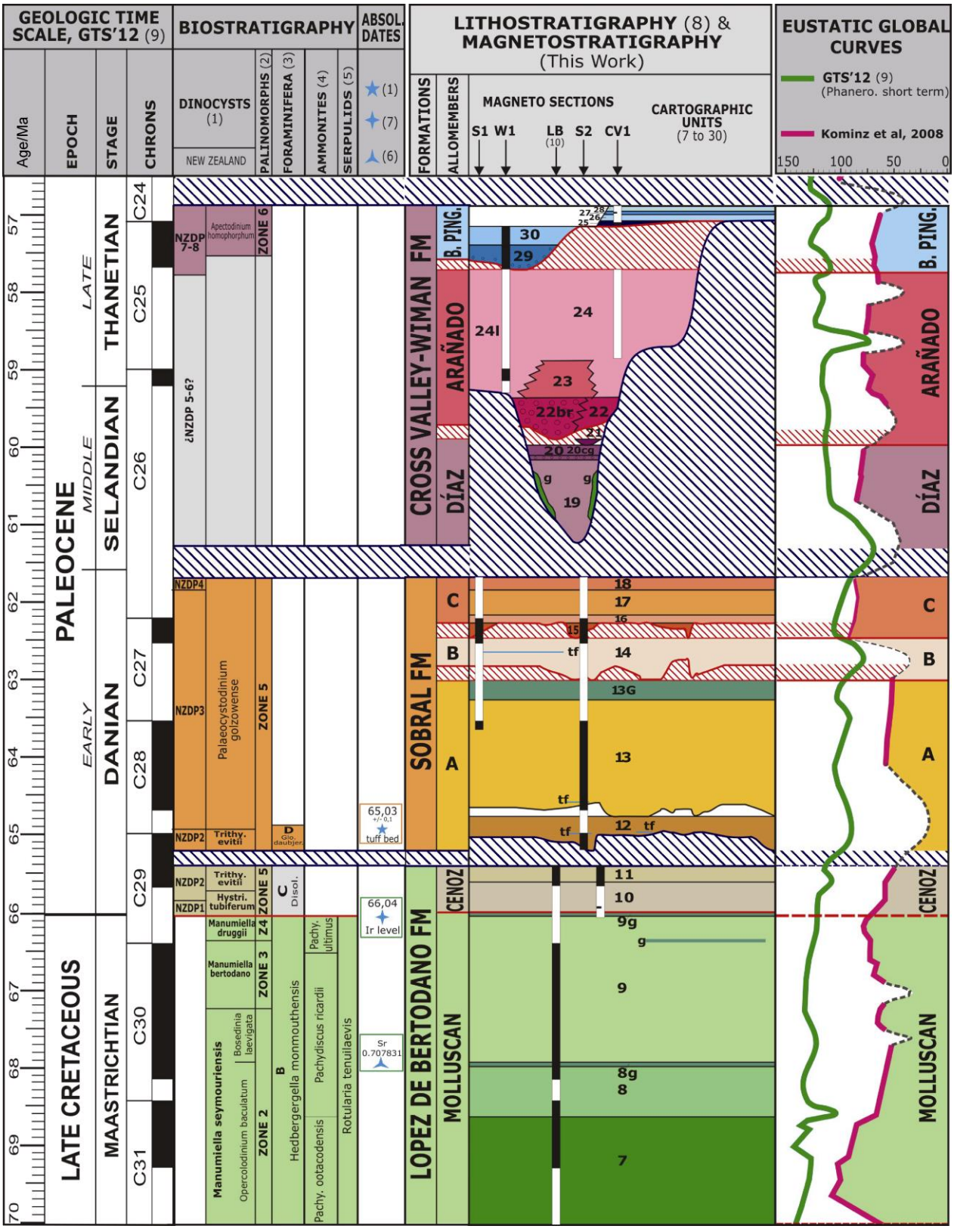

Figure 10 Chronostratigraphic framework and age model in Ma of the late Maastrichtian–Paleocene from Seymour Island, with the main litho-, bio-, chemo- and magnetostratigraphic content. The erosive surfaces that limit different stratigraphic units are related to abrupt drops in sea level. References: (1) Bowman et al. (2016); (2) Askin (1988); (3) Huber (1988); (4) Olivero and Medina (2000); (5) Macellari (1988); (6) Crame et al. (2004); (7) Elliot et al. (1994); (8) Montes et al. (2013, 2019); (9) Grandstein et al. (2012); (10) Tobin et al. (2012).

As the eustatic curve for these units shows a stable sea level, the observed siliciclastic progradational facies would occur in a context of increased sedimentation rate. This increase is observed in the sedimentation rate curve (20.0 cm·ka^{-1}, Figure 9).

5.3 Cross Valley Wiman Formation (CVWF): Selandian–Thanetian

The basal discontinuity of CVWF is a large erosive surface that produces an incised valley of steep slopes. This surface should correspond to an appreciable relative drop in sea level, coinciding with the one observed between 61–62 Ma in the eustatic curves. This large drop in global sea level is used, among others, for definition of the lower limit of Selandian (61.6 Ma, Vanderberghe et al., 2012). According to this correlation, the base of the CVWF would coincide with the beginning of Selandian (Figures 9 and 10).

In the Cross Valley area, the erosive surface is incised more than 200 m. However, the eustatic curves show a fall of ~40 m, insufficient for the magnitude of incision (Figure 9). These observations imply that erosion of the incised valley had to occur with a combined process of platform emersion and sea level fall. In this sense, the airfall tuffs present in SF, indicate an active volcanism during Danian in the Antarctic Peninsula magmatic arc. The strong incision of the canyon and the later infilling by coarse volcanoclastic deposits with abundant remains of burned fossil wood, suggest a strong increase in volcanic activity and uplift of magmatic arc synchronic with the CVWF sedimentation.

The incised valley would begin to be filled with coarse vulcanoclastic material from the Díaz Allomember base (unit 19). Simultaneously, the upper edges of the palaeochannel would be above the top of the deposits and therefore exposed to a very low sedimentation rate favorable to formation of autochthonous glauconite. Glauconite presence at upper edges of actual submarine canyons has been previously reported (Hein et al., 1974). Subsequently, the walls of the canyon with presence of glauconite would be onlapped by successive sediments of the Díaz Allomember.

The following sedimentary cycles (20cg, 20, 21), imply a widening of the canyon, (400–600 m) with erosion and filling (Figures 2 and 4). Eustatic curve is stable for these units (Figure 9), so cycles of erosion and filling must be interpreted by changes in subsidence and/or sedimentation rate.

The Arañado Allomember (22br, 22, 23), would represent another episode of erosion-sedimentation with more energy than the previous ones (Arañado Hill breccias, 22br) and the culmination of infilling the canyon deepest zone. This fact is argued for the overflow of unit 24 on more confined part of the incised valley extending its width and producing the paraconformity with upper beds of SF (TPs5 by Sadler, 1988). In addition, sedimentary characteristics of the upper part of the allomember (23, 24), would indicate an estuarine deposit environment with tidal influence. Facies in Cape Wiman outcrop (planar and trough cross-bedding lamination, 24l) are also indicative of a strong tidal influence.

The lower limit of the Arañado Allomember would correspond to a descent ~60 Ma, according to eustatic curves (Figures 9 and 10). However, coarse volcanoclastic deposits would imply also an uplift in the source area. The overflow of incised valley (23, 24, TPs5), would occur with a rising sea level between Selandian and Thanetian (~C26n; ~59 Ma).

Bahía Pingüino Allomember (25–30), presents a substantial change in facies and clastic composition. In Cross Valley outcrops, two observed sequences (25–27; 26–28), are interpreted as lagoon facies or protected bay near coast (dark shales with ostreas), with occasional detritic sediments (sandstones). High content of paleobotanical remains and the allomember base channel morphology, would indicate tractive currents from NE–SW direction, no longer confined according to the main direction of the incised valley (NW–SE). Overall, the sedimentation rate for the CVWF is lower than for the SF with 5.5 cm·ka^{-1} (Figure 9).

Changes in composition of volcanic to siliciclastic detritical clast (Elliot and Hoffman, 1989), may indicate that erosive level reached the basement of the volcanic arc zone (Antarctic Peninsula) once the contemporary volcanic buildings to SF and Díaz were eroded (Marenssi et al., 2012).

Cape Wiman palaeochannel (29, 30), is related to a descent of the eustatic curve of ~57.7 Ma (GTS'12) (Figures 9 and 10). The base of sequences of dark shales with ostreas and laminated sandstones (25–27; 26–28), corresponds to eustatic descent of ~57 Ma. Units 29 and 30 in Cape Wiman have been interpreted as the filling of a palaeochannel with an E–W orientation, with mixed volcanic-siliciclastic sediments, similar to the Bay Penguin Allomember in the Cross Valley area. La Meseta Formation (Eocene) separates both outcrops, which makes impossible determining whether the Wiman deposits would belong to a contemporary palaeochannel but different from the incised valley of Cross Valley, or it would be the same.

6 Conclusions

The new magnetostratigraphic data of the Cenozoic sediments of the James Ross Basin together with the previous (1) lithostratigraphy: recently redefined stratigraphic units and high resolution geological mapping; (2) biostratigraphy: dinoflagellate cyst, palynomorphs, foraminifera; (3) chemostratigraphy: Iridium anomaly (K-Pg boundary), U-Pb dating of zircons (airfall tuff), strontium isotope values from macrofossils; and (4) magnetostratigraphic studies (lower units of LBF); have led

to a new chronostratigraphy, that substantially changes and precise the traditionally accepted ages. This new chronostratigraphic framework provides a robust stratigraphic context for these reference outcrops of the early Cenozoic from Antarctica.

The LBF, SF and CVWF, are unconformity-bounded units (alloformations) that record the geological evolution of the James Ross Basin during a period of relative decreasing tectonism but with volcanic activity. Unconformity based internal units have been recognized, dividing each formation in allomembers: LBF: Molluscan and Cenozoic allomembers; SF: A, B and C allomembers; and CVWF: Díaz, Arañado and Bahía Pingüino allomembers.

The upper part of the LBF is confirmed as Maastrichtian at earliest Danian age (~65.4 Ma). The overlaying SF is mostly Danian in age (~65.2– ~63 Ma) and CVWF is Selandian–Thatenian in age (~61.3–56.9 Ma).

The new model allows the correlation of base level changes with eustatic fluctuations in sea level. The limit between the Molluscan and Cenozoic allomembers of LBF is observed in upper part of beds rich in glauconite, where the Iridium anomaly of K-Pg boundary has been found (66.04 Ma). These levels rich in autochthonous glauconite are interpreted as maximum flooding surface deposits that culminate a transgressive sequence, started at the base of Molluscan Allomember. Consequently, this limit can be also considered as a sequence boundary.

The base of the SF is correlated with 65.3 Ma lowstand in sea level. Two limits between SF allomember (A–B and B–C), coincided with ~62.9 and ~62.5 Ma lowstand. Magnitudes for both erosive surfaces, are coherent with meters of eustatic sea level drop. However, not all the erosive surfaces observed within SF units, can be related to sea level fluctuations (unit 13 base). Changes in basin subsidence originated by Antarctic Peninsula uplift, would be the explanation.

The base of the CVWF is correlated with 61.5 Ma, (well-known limit of Selandian) drop in global sea level curves. The incision of the erosive surface is more than 200 m, much higher than eustatic fall (~40 m). In this case, a combined process of platform emersion and sea level fall is suggested. In this sense, the airfall tuffs present in SF (65.05±0.15 Ma) indicate an active volcanism that already began, from the Antarctic Peninsula magmatic arc in Danian times. The strong incision and its subsequent filling by thick volcanoclastic deposits with abundant remains of burned fossil wood, suggests a strong increase of volcanic activity and magmatic arc uplift, synchronic with CVWF sedimentation.

Changes in the composition of volcanic to siliciclastic detritical clasts observed between Arañado and Bahía Pingüino Allomember (~57.7 Ma lowstand), may indicate that the erosive level reached the basement of the area of the volcanic arc (Antarctic Peninsula) once the volcanic buildings concurrent to SF and Díaz Allomember were eroded. By the end of Arañado Allomember deposition, the incised valley was totally overfilled and the beds of CVWF overlapped on top of SF (18). This fact clarifies that Tps5 (by Sadler, 1988) does not belong to SF but to Arañado (24) and to Bahía Pingüino (25–28) allomembers. The gap in the dinoflagellate cyst biostratigraphy (absence of NZDP5–6 biozones), detected by Bowman et al. (2016) at top of SF, would coincide with the deposition of the Díaz Allomember (Selandian–early Thanetian).

Correlation of Paleocene sea-level fluctuations in the northern Antarctic Peninsula (James Ross Basin) with the global sea-level curve strengthens, in general, the concept of global synchronicity of the eustatic sea-level curve, although with some peculiarities. The presence of peaks in abundance of cold water dinoflagellate in Moluscan Allomember (unit 8), could indicate the existence of glaciers in higher levels in Antarctic continent already in Cretaceous times and also, local or even global, glacio-eustatic phenomena.

Acknowledgments The authors are most grateful to the DNA-Instituto Antártico Argentino for the scientific and logistic support during the Argentine Summer Antarctic Expeditions 2009–2011. This work was supported by the Instituto Geológico y Minero de España (IGME) and Dirección General de Investigación (DGI) from Spain by the projects CTM2011-30241-C02-02 and CTM2014-60451-C2-2-P. The authors want to thank the Geomodels Research Institute and the Grup de Recerca de Geodinàmica i Anàlisi de Conques (Grant no. 2017SGR596, supported by AGAUR). We thank the Paleomagnetic Laboratory of Barcelona (CCiTUB-ICTJA CSIC) where the palaeomagnetic analyses were carried out.

References

Amorosi A. 1995. Glaucony and sequence stratigraphy; a conceptual framework of distribution in siliciclastic sequences. J Sed Res, 65: 419-425

Askin R. 1988a. Campanian to Paleocene palynological succession of Seymour and adjacent islands, northeastern Antarctic Península// Feldman R, Woodbume M. Geology and Paleontology of Seymour Island, Antarctic Peninsula. Geol Soc Am Mem, 169: 131-153.

Askin R A. 1988b. The palynological record across the Cretaceous/Tertiary transition on Seymour Island, Antarctica// Feldman R, Woodbume M. Geology and Paleontology of Seymour Island, Antarctic Peninsula. Geol Soc Am Mem, 169: 155-162.

Bohoyo F. 2004. Fragmentación continental y desarrollo de cuencas oceánicas en el sector meridional del Arco de Scotia, Antártida. Tesis Doctoral, Universidad de Granada.

Bowman V, Francis J, Riding J, et al. 2012. A latest Cretaceous to earliest Paleogene dinoflagellate cyst zonation from Antarctica, and implications for phytoprovincialism in the high southern latitudes. Rev Palaeobot Palyno, 171: 40-56.

Bowman V, Francis J, Riding J. 2014a. Late Cretaceous winter sea ice in Antarctica? Geology, 41: 1227-1230, doi: 10.1130/G34891.1.

Bowman V, Francis J, Askin R, et al. 2014b. Latest Cretaceous–earliest

Paleogene vegetation and climate change at the high southern latitudes: palynological evidence from Seymour Island, Antarctic Peninsula. Palaeogeog Palaeoclim Palaeoecol, 408: 26-47, doi: 10.1016/j.palaeo. 2014.04.018.

Bowman V, Ineson J, Riding J, et al. 2016. The Paleocene of Antarctica: Dinoflagellate cyst biostratigraphy, chronostratigraphy and implications for the palaeo-Pacific margin of Gondwana. Gondwana Res, 38: 132-148, doi: 10.1016/j.gr.2015.10.018.

Courtillot V, Fluteau F. 2010. Cretaceous extinctions: the volcanic hypothesis. Science, 328: 973-974.

Crame J, Beu A, Ineson J, et al. 2014. The early origin of the Antarctic marine fauna and its evolutionary implications. PloS ONE, 9(12): e114743, doi: 10.1371/journal.pone. 0114743.

Crame J, Francis J, Cantrill D, et al. 2004. Maastricthian stratigraphy of Antarctica. Cret Res, 25: 411-423.

Del Valle R, Elliot O, Mcdonald O. 1992. Sedimentary basins of the east flank of the Antarctic Peninsula: proposed nomenclature. Antarc Sci, 4: 477-478.

Elliot D, Askin R, Kyte F, et al. 1994. Iridium and dynocist at the Cretaceos–Tertiary boundary on Seymour Island, Antarctica: Implications for the K/T event. Geology, 22: 675-678.

Elliot D, Hoffman S. 1989. Geologic studies on Seymour Island. Antarctic Journal of the United States, 24(5): 3-5.

Elliot D, Trautman T. 1982. Lower Tertiary strata on Seymour Island, Antarctic Peninsula//Craddock C. Antarctic Geoscience. Madison: University of Wisconsin Press, 287-297.

Gradstein F, Ogg J, Schmitz M, et al. 2012. The Cronostratigraphic Scale//Gradstein F, Ogg J, Schmitz M, et al. The geologic time scale 2012, Elservier, 31-42, doi: 10.1016/B978-0-444-59425.00002-0.

Harris L, Whiting B. 2000. Sequence-stratigraphic significance of Miocene to Pliocene glauconite-rich layers on and offshore of the US Mid-Atlantic margin. Sed Geol, 134 (1-2): 129-147.

Harwood D. 1988. Upper Crettaceous and lower Paleocene diatom and silicoflagellate biostratigraphy of Seymour Island, eastern Antarctic Peninsula//Feldman R, Woodbume M. Geology and paleontology of Seymour Island, Antarctic Peninsula. Geol Soc Am Mem, 169: 55-129.

Hathway B. 2000. Continental rift to back-arc basin: Jurassic–Cretaceous stratigraphical and structural evolution of the Larsen Basin, Antarctic Peninsula. J Geol Soc Lond, 157: 417-432.

Hein J, Allwardt A, Giggs G. 1974. The occurrence of glauconite in Monterrey Bay, California: diversity, origins, and sedimentary environmental significance. J Sediment Petrol, 44(2): 562-571.

Hoffman S. 1991. Petrology and provenance of the Paleocene strata at Cape Wiman, Seymour Island (Antarctic Peninsula). Unpublished Thesis MSc. The Ohio State University, USA.

Huber B. 1988. Upper Campanian–Paleocene foraminifera from the James Ross Island region, Antarctic Peninsula//Feldman R, Woodbume M. Geology and Paleontology of Seymour Island, Antarctic Peninsula. Geol Soc Am Mem, 169: 163-252.

Kirshvinck J. 1980. The least-squares line and plane and the analysis of paleomagnetic data. Geophys J Int, 62: 699-718.

Kominz M, Browning J, Miller K, et al. 2008. Late Cretaceous to Miocene sea-level estimates from the New Jersey and Delaware coastal plain coreholes: an error análisis. Basin Res, 20: 211-226.

Lowrie W. 1990. Identification of ferromagnetic minerals in a rock by coercivity and unblocking temperature properties. Geophys Res Lett, 17(2): 159-162.

Macellari C. 1986. Late Campaniane Maastrichtian ammonite fauna from Seymour Island (Antarctic Peninsula). Memoir of Paleontological Society, 18: 1-55.

Macellari C. 1988. Stratigraphy, sedimentology, and paleoecology of Upper Cretaceous/Paleocene shelf-deltaic sediments of Seymour Island//Feldman R, Woodbume M. Geology and paleontology of Seymour Island, Antarctic Peninsula. Geol Soc Am Mem, 169: 25-53.

Marenssi S, Net L, Santillana S. 2002. Provenance, enviromental and paleogeographic controls on sandstone composition in an incised valley system: the Eocene La Meseta Formation, Seymour Island, Antactica. Sed Geol, 150: 301-321.

Marenssi S, Santillana S, Bauer M. 2012. Estratigrafía, petrografía sedimentaria y procedencia de las formaciones Sobral y Cross Valley (Paleoceno), isla Marambio (Seymour), Antártica. Andean Geology, 39(1): 67-91.

Marenssi S A, Santillana S N, Rinaldi C A. 1998a. Paleoambientes sedimentarios de la Aloformación La Meseta (Eoceno), Isla Marambio (Seymour), Antártida. Instituto Antártico Argentino, Contribución, 464: 1-51.

Marenssi S, Santillana S, Rinaldi C. 1998b. Stratigraphy of La Meseta Formation (Eocene), Marambio Island, Antarctica//Casadío S. Paleógeno de América del Sur y de la Península Antártica. Revista de la Asociación Paleontológica Argentina, Publicación Especial, 5: 137-146.

Martin J, Fernández M. 2007. The Synonymy of the Late Cretaceous Mosasaur (Squamata) Genus Lakumasaurus from Antarctica with Taniwhasaurus from New Zealand and its bearing upon faunal similarity within the Weddellian Province. Geol J, 42: 1-9.

Martos Y, Catalán M, Galindo-Zaldívar J, et al. 2014. Insights about the structure and evolution of the Scotia Arc from a new magnetic data compilation. Global Planet Change, 123: 239-248.

Mcarthur J, Thirlwall M, Engkilde M, et al. 1998. Strontium isotope profiles across K/T boundary sequences in Denmark and Antarctica. Earth Planet Sci Lett, 160: 179-192.

Molina E. 2015. Evidence and causes of the main extinction events in the Paleogene based on extinction and survival patterns of foraminifera. Earth-Sci Rev, 140: 166-181.

Montes M, Nozal F, Olivero G, et al. 2019. Geología y Geomorfología de la isla Marambio (Seymour). Serie Cartográfica Geocientífica Antártica; 1:20.000, 1ª edición. Acompañado de mapas. Madrid-Instituto Geológico y Minero de España; Buenos Aires-Instituto Antártico Argentino, 250.

Montes M, Nozal F, Santillana S, et al. 2013. Mapa Geológico de la isla de Marambio (Seymour); escala 1:20.000. 1º edición. Serie Cartográfica Geocientífica Antártica. Con texto complementario. Madrid-Instituto Geológico y Minero de España; Buenos Aires-Instituto Antártico Argentino.

Montes M, Santillana S, Nozal F, et al. 2008a. Estratigrafía de la Formación Sobral. Paleoceno inferior de la Isla Marambio. (Mar de Weddell, Antártida). Geo-Temas, 10: 669-672.

Montes M, Santillana S, Nozal F, et al. 2008b. El Paleoceno superior de la Antártida: la Formación Cross Valley-Wiman de la Isla Marambio. (Mar de Weddell). Geo-Temas, 10: 667-668.

Odin G S. 1988. Green marine clays: Oolitic Ironstone Facies, Verdine

Facies, Glaucony Facies and Celadonite-Bearing Rock Facies–A comparative study. Development in sedimentology, 45. Amsterdam: Elsevier.

O'keefe F, Otero R, Soto-Acuña S, et al. 2017. Cranial anatomy of Morturneria seymourensis from Antarctica, and the evolution of filter feeding in plesiosaurs of the Austral Late Cretaceous. J Vertebr Paleontol, 37: 4, doi: 10.1080/ 02724634.2017.1347570.

Olivero E. 2012. Sedimentary cicles, ammonite diversity and paleoenviromental changes in the upper cretaceous Marambio Group, Antarctica. Cret Res, 34: 348-366, doi: 10.1016/j.cretres.2011.11.015.

Olivero E, Medina F. 2000. Patterns of Late Cretaceous ammonite biogeography in southern high latitudes: the Family Kossmaticeratidae in Antarctica. Cret Res, 21: 269-279.

Olivero E, Ponce J, Marsicano C, et al. 2007. Depositional settings of the basal López de Bertodano Formation, Maastrichtian, Antarctica. Revista de la Asociación Geológica Argentina, 62: 521-529.

Olivero E, Ponce J, Martinioni D. 2008. Sedimentology and architecture of sharp-based tidal sandstones in the Upper Marambio Group, Maastrichtian of Antarctica. Sed Geol, 210: 11-26.

Olivero E, Raffi M, Bedoya E, et al. 2017. Discovery of fossiliferous breccias at the K-Pg boundary and upper López de Bertodano Formation, Antarctica: paleoenvironmental interpretation. 9° Congreso Latinoamericano de Ciencia Antártica. Punta Arenas, Chile.

Pirrie D, Whitham A, Ineson J. 1991. The role of tectonics and eustacy in the evolution of a marginal basin: Cretaceous–Tertiary Larsen Basin, Antarctica//Macdonald D. Sedimentation, tectonics and eustacy: Sea level changes at active margins. International Association of Sedimentologists, Special Publications, 12: 293-305.

Rinaldi C, Massabie A, Morelli J, et al. 1978. Geología de la isla Vicecomodoro Marambio, Antártida. Instituto Antártico Argentino Contribución, 217: 1-37.

Royer D. 2006. CO_2-forced climate thresholds during the Phanerozoic. Geochim Cosmochim Ac, 70: 5665-5675.

Sadler P. 198). Geometry and stratification of uppermost Cretaceous and Paleogene units on Seymour Island, northern Antarctic//Feldman R, Woodbume M. Geology and paleontology of Seymour Island, Antarctic Peninsula. Geol Soc Am Mem, 169: 303-320.

Santillana S, Montes M, Nozal F, et al. 2007. Secuencias Estratigráficas de la Fm Sobral (Paleoceno inferior) de la isla Marambio. Península Antártica. Buenos Aires, Argentina. VI Simposio Argentino y III Latinoamericano sobre Investigaciones Antárticas. Comunicaciones. CDROM: GEOR E829.

Schoene B, Samperton K M, Eddy M P, et al. 2015. U-Pb geochronology of the Deccan Traps and relation to the end-Cretaceous mass extinction. Science, 347(6218): 182-184, doi: 10.1126/science.aaa0118.

Schulte P, Alegret L, Arenillas I, et al., 2010. The Chicxulub asteroid impact and mass extinction at the Cretaceous–Paleogene boundary. Science, 327: 1214-1218.

Tambussi C, Reguero M, Marenssi S, et al. 2005. Crossvallia unenwillia, a new Spheniscidae (Sphenisciforme, Aves) from late Paleocene of Antarctica. Geobios, 172: 1-9.

Tobin T, Ward P, Steig E, et al. 2012. Extinction patterns, ^{18}O trends, and magnetostratigraphy from a southern high-latitude Cretaceous-Paleogene section: Links with Deccan volcanism. Palaeogeog Palaeoclim Palaeoecol, 350-352: 180-188, doi: 10.1016/j.palaeo.2012.06.029.

Vandenberghe N, Hilgen F, Speijer R. 2012. The Paleogene period//Gradstein F, Ogg J, Schmitz M, et al. The geologic time scale 2012. Elsevier, 855-921, doi:10.1016/B978-0-444-59425-9.00028-7.

Wrenn J, Hart G. 1988. Paleogene dinoflagellate cyst biostratigraphy of Seymour Island, Antarctica//Feldman R, Woodbume M. Geology and paleontology of Seymour Island, Antarctic Peninsula. Geol Soc Am Mem, 169: 321-447.

Zachos J, Dickens G, Zeebe R. 2008. An early Cenozoic perspective on greenhouse warming and carbon-cycle dynamics. Nature, 451: 279-283.

Zachos J, Pagani M, Sloan L, et al. 2001. Trends, rhythms, and aberrations in global climate 65 Ma to present. Science, 292: 686-693.

Table 1 Excel file with paleomagnetic directions. Site/sample: name of the sample. Relative level: position in the stratigraphic section. Ds, Is: declination and inclination after tectonic correction. Plat: paleolatitude. Int: intensity of the component. Error: error of the calculated component (which is MAD: maximum angular deviation). *Q*: quality of the component (1: good to 3: bad). Trange: temperature range over which component was calculated. Trange ChComp: temperature steps considered for the calculation of the characteristic component; "*" indicating that characteristic component is calculated without including the origin. Treatment: demagnetization treatment used; TH: thermal; AF: alternating field. The grey shading indicates samples with $Q \geq 3$

Site/sample	Relative level/m	Ds	Is	Latp	Int/(10^{-6}A·m^{-1})	Error	*Q*	Trange	Trange ChComp	Treatment
CV-00-1A	0	183.0224	44.84745	−52.14	389.83	9.31	2	3	200–320	TH
CV1-01	0.5	184.2062	70.99329	−80.94	1475.37	12.49	2	4	20–40	AF
CV1-02	5	217.7008	−33.79946	−2.3	861.27	7.98	2	5	30–50	AF
CV1-03	10	229.6935	−1.49523	−15.62	114.32	25.16	2	1	60–100	AF
CV1-05	19	178.1659	−24.8238	−12.71	75.02	12.06	2	6	40–60	AF
CV1-06	23	110.2109	40.6126	−29.53	83.17	9.39	2	1	80–120	AF
CV1-08	28	111.8869	4.026035	−11.16	90.73	2.83	2	8	60–80	AF
CV102-1A	28	33.74832	−39.1423	42.38	183.54	15.17	2	3	280–330	TH
CV103-1B	29	16.22032	23.54016	12.47	1543.04	6.61	2	3	310–390	TH
CV1-09	32	186.1673	73.3942	−84.16	93.67	9.57	2	6	50–60	AF
CV-09-1A	32	181.9277	52.424	−58.74	337.63	11.08	2	3	*250–350	TH
CV1-10	35	13.66504	63.26825	−19.57	321.39	13.28	2	1	30–100	AF
CV-10-2A	35	26.76159	55.04512	−12.03	745.67	10.00	2	3	290–380	TH
CV-11-1A	36.5	133.549	65.60819	−60.26	2772.85	6.23	2	2	150–200	TH
CV1-11	36.5	222.6193	50.42336	−47.71	244.51	31.07	2	1	*30–100	AF
CV1-12	38.5	16.66872	−25.97005	38.13	278.49	4.93	1	8	*40–80	AF
CV-14-1A	41	136.1927	47.06374	−44.63	1626.49	6.40	2	4	380–420	TH
CV1-07	26	210.7156	−49.22163	7.39	78.81	15.65	3	8	60–80	AF
CV105-1A	31.5	91.55561	29.97036	−15.12	486.44	5.78	3	3	200–330	TH
W-3ACA	7	102.3203	34.94168	−22.62	151.03	9.00	2	4	350–410	TH
W-5BCA	13	316.4763	−40.53522	39.93	70.67	40.83	2	4	*250–410	TH
W-6ACA	19	140.2596	52.86185	−50.81	350.15	4.86	2	4	350–410	TH
W-7ACA	23	75.6018	−27.21124	19.2	1268.21	3.14	1	5	290–500	TH
W-23AA	81	319.1642	−71.23303	68.39	437.57	3.90	2	3	150–290	TH
W-25AA	88	336.2816	−45.24425	49.53	602.44	3.81	2	5	350–500	TH
W-27AA	93	320.5725	−7.369578	22.96	307.75	3.05	2	2	200–290	TH
W-20AA	72	83.07395	−34.50967	20.02	355.93	3.69	3	2	150–200	TH
S1-27AA	75.5	142.5476	37.4585	−40.11	49.06	10.73	2	3	200–290	TH
S1-30AA	81	142.1539	22.05481	−31	131.22	6.71	2	4	410–440	TH
S1-46AA	122	30.94064	−55.81479	56.52	214.22	8.97	2	4	320–470	TH
S1-47AA	126	19.47727	−54.48032	58.45	169.61	11.41	2	4	250–440	TH
S1-54AA	144	147.2898	38.92648	−42.37	73.22	4.08	2	3	290–320	TH
S1-67AA	181	295.2962	−10.18194	15.39	77.55	14.59	2	3	150–290	TH
S1-75AA	209	18.40641	−11.26803	29.97	279.19	7.57	2	4	350–470	TH
S1-78AA	217	143.7437	24.33562	−32.71	94.93	14.52	2	4	350–440	TH
S1-83AB	228	307.245	−63.16919	55.1	443.53	6.79	2	3	200–350	TH
S1-13AA	32	46.54607	−33.80622	34.7	138.94	18.23	3	3	250–320	TH
S1-21-2A	56.5	156.2555	55.97985	−58.83	95.62	11.17	3	3	200–290	TH
S1-29BA	79	121.9047	19.04914	−22.3	145.02	11.41	3	3	200–290	TH

Continued

Site/sample	Relative level/m	Ds	Is	Latp	Int/(10^{-6}A·m^{-1})	Error	*Q*	Trange	Trange ChComp	Treatment
S1-35AA	93	320.0345	−37.17647	39.1	91.74	21.48	3	3	290–380	TH
S1-40CA	107	33.00859	−9.955029	26.21	153.36	9.10	3	3	290–350	TH
S1-41BA	109	42.28114	−52.29591	49.38	109.35	17.70	3	3	*200–320	TH
S1-49BA	134	249.361	28.29437	−22.4	205.47	6.06	3	4	380–470	TH
S1-61BA	164	312.6591	−51.74065	46.96	170.78	4.76	3	3	150–290	TH
S1-89CB	246	63.89517	−22.44557	21.68	128.78	9.95	3	3	*100–320	TH
S2-01-1A	0	161.8162	54.52862	−58.57	351.24	18.50	2	3	290–380	TH
S2-03-1A	4.5	197.0426	30.97203	−40.82	567.12	3.54	2	3	320–350	TH
S2-04-1A	7	38.31967	−56.21173	54.18	689.97	12.88	2	2	200–320	TH
S2-05-1A	10	191.2094	71.43575	−79.97	2073.35	8.39	2	4	200–420	TH
S2-06	13	12.513	−2.192548	25.94	332.50	6.44	2	4	10–40	AF
S2-07-1A	16	68.62604	−31.3723	24.41	1978.20	6.80	1	4	250–420	TH
S2-08-1A	19	186.6627	70.91956	−80.25	734.02	10.90	2	3	250–290	TH
S2-11-3A	29	203.4488	3.16848	−24.82	309.73	1.28	2	3	250–290	TH
S2-12-1A	31	333.0547	−15.44079	30.24	699.24	8.81	2	3	250–320	TH
S2-15-1A	41	186.9046	12.9696	−31.86	265.89	6.87	2	3	250–290	TH
S2-19-1A	51	226.93	26.52472	−30.25	242.94	11.77	2	3	290–350	TH
S2-20	52.5	306.4671	−32.92295	31.43	385.73	8.39	2	6	10–60	AF
S2-22-1A	58.5	5.457901	−40.23395	48.28	1104.49	13.03	2	3	*200–350	TH
S2-26-3A	70	44.55902	13.10576	11.56	439.66	5.52	2	3	250–320	TH
S2-30-3A	82	18.07417	−45.2021	50.49	190.52	12.52	2	2	200–250	TH
S2-32-1A	88	52.01252	−57.44574	49.92	3007.90	4.34	1	4	200–460	TH
S2-35-1A	97	91.06083	42.13266	−22.29	123.35	9.36	2	3	200–380	TH
S2-39-3B	109	44.78563	−48.12849	44.95	111.28	12.65	2	3	200–350	TH
S2-43-3A	128	116.978	−44.49845	12.87	373.03	5.72	2	3	250–320	TH
S2-47-1A	144.5	121.0883	−27.33235	0.61	199.52	14.20	2	3	290–3350	TH
S2-48-1A	146	127.9896	40.91796	−37.02	42.47	31.82	2	4	420–440	TH
S2-49-1A	149	218.8415	44.33613	−44.23	267.50	11.64	2	3	200–350	TH
S2-50-2A	150.5	159.201	63.8578	−67.83	93.01	40.87	2	4	350–400	TH
S2-51-3A	155	92.72697	2.73955	−2.41	1060.92	4.01	1	4	250–440	TH
S2-52-1B	157	10.16127	−52.50383	57.98	95.10	39.05	2	3	*200–350	TH
S2-61-3A	187	197.3906	2.662371	−25.58	325.17	0.44	2	4	*350–400	TH
S2-62-1A	190	136.406	10.82885	−23.35	505.83	9.52	2	3	290–380	TH
S2-63	192.5	125.6653	−7.537563	−11	67.66	3.63	2	4	40–60	AF
S2-65-1A	198.5	157.435	79.29516	−80.01	376.44	4.99	2	3	290–380	TH
S2-68-1A	206.5	36.08232	26.3644	6.93	458.28	10.74	2	3	250–350	TH
S2-69	208	237.5565	26.68077	−26.36	117.74	15.08	2	6	50–60	AF
S2-70-1A	209	19.17941	−34.61216	42.75	98.51	9.68	2	3	*200–320	TH
S2-71-3A	211	55.27597	31.73688	−1.86	186.59	4.38	2	3	200–320	TH
S2-72-1A	215	43.56746	30.95066	2.27	104.61	22.60	2	3	290–350	TH
S2-78-1A	240	171.7799	−38.38947	−3.65	3024.59	8.00	1	4	290–380	TH
S2-79-1A	244	162.4704	−0.1636943	−24.16	1066.17	12.95	2	3	250–320	TH
S2-80-1A	249	21.31024	14.99264	16.13	2159.18	6.74	2	4	320–440	TH
S2-81-1A	253	331.3807	13.04904	15.75	436.01	4.18	1	4	250–420	TH

Continued

Site/sample	Relative level/m	Ds	Is	Latp	Int/(10^{-6}A·m^{-1})	Error	*Q*	Trange	Trange ChComp	Treatment
S2-82-1A	256	348.6724	−23.46289	37.15	268.55	22.51	2	4	*290–400	TH
S2-83-1A	258	155.3643	40.24568	−45.41	794.39	12.23	2	4	290–400	TH
S2-87-1A	278.5	321.2257	62.28855	−22.28	1832.52	9.15	2	4	320–460	TH
S2-88-1A	283	210.2109	11.98953	−27.73	943.55	21.07	2	3	250–350	TH
S2-89-2A	288	209.6418	54.26923	−55.32	278.61	6.30	1	4	200–380	TH
S2-90-1A	292	109.8319	−33.19377	8.15	855.23	8.96	2	3	250–380	TH
S2-92-1A	301.5	127.3801	10.9617	−20.31	288.59	10.80	2	4	400–440	TH
S2-94-1A	312	63.6543	−41.61763	32.75	1141.87	7.13	2	3	320–380	TH
S2-96-1A	320.5	89.20159	−65.1769	41.81	498.62	9.59	2	3	250–380	TH
S2-97-1A	325	330.821	46.62834	−5.16	976.31	5.57	2	4	350–440	TH
S2-09-1A	22	100.6505	−4.79812	−2.39	1225.29	4.04	3	2	200–250	TH
S2-25-1A	67.5	131.257	23.55978	−28.01	299.19	4.59	3	2	200–250	TH
S2-33-31	91	126.4398	21.1241	−24.98	104.44	25.65	3	2	200–250	TH
S2-34-1A	94	358.0038	−30.95814	42.18	107.61	19.97	3	2	200–250	TH
S2-41-3A	119	2.829935	−44.73942	51.81	185.56	7.54	3	2	200–250	TH
S2-42-3A	123.5	61.30958	−42.70965	34.46	208.91	1.72	3	2	200–250	TH
S2-60-1A	186	166.7967	36.66425	−45.04	866.21	10.39	3	2	200–250	TH
S2-29-3A	79	115.3643	18.55947	−19.35	205.50	15.70	3	3	290–300	TH
S2-40-3A	114	185.3934	−62.86246	18.87	144.24	1.30	3	3	290–320	TH
S2-64-1A	195.5	258.4504	52.486	−34.39	332.81	3.96	3	3	290–320	TH
S2-66-1A	200.5	183.2818	6.775308	−28.85	426.62	8.27	3	3	*290–380	TH
S2-74-1A	224	100.5847	−42.80823	17.91	84.35	27.19	3	3	*250–320	TH
S2-84-1A	263	126.4153	46.46343	−40.28	504.83	15.40	3	3	290–320	TH

Appendix

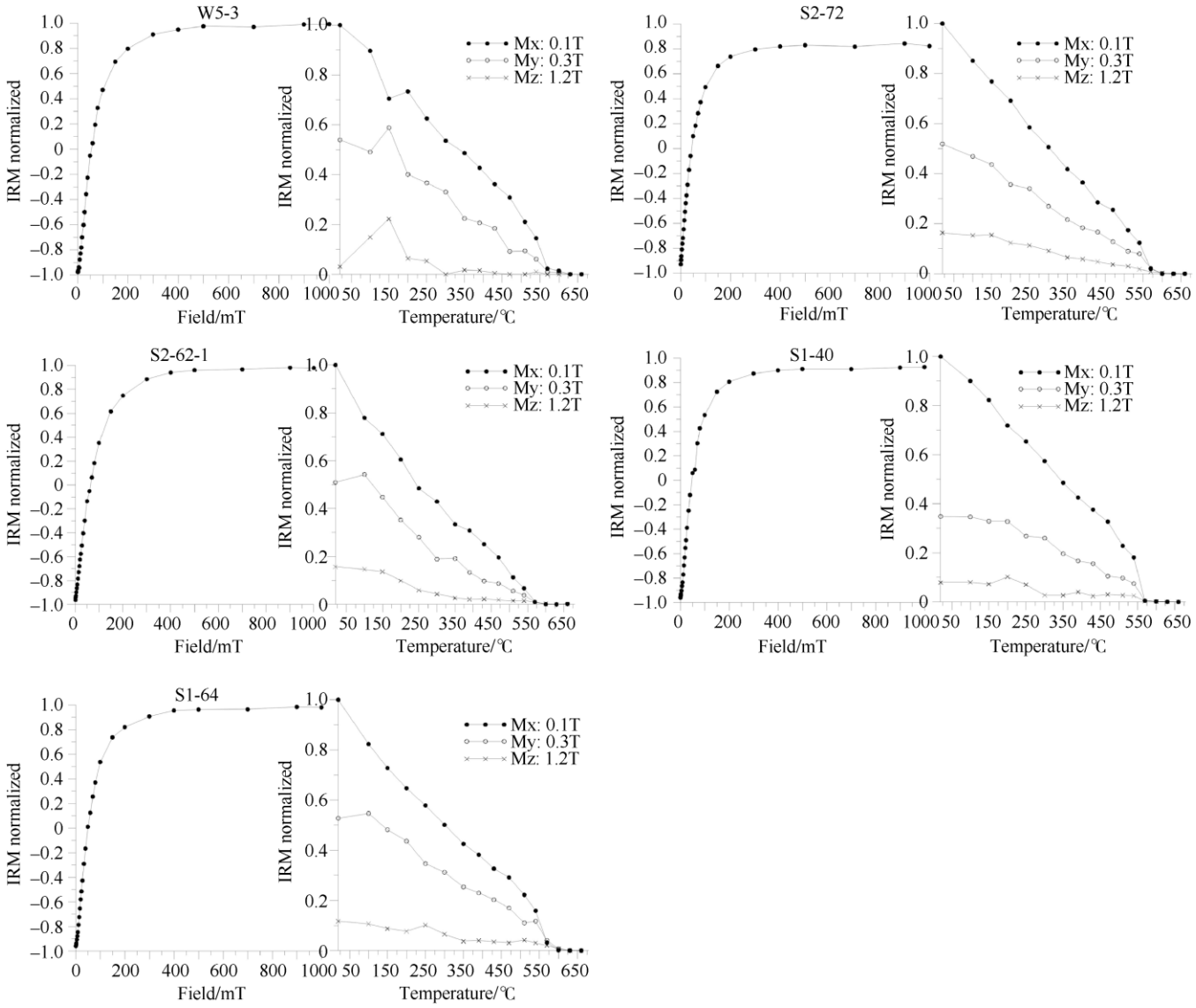

Figure A1 IRM acquisition (left) and 3 axes IRM demagnetization (right) of selected samples of the Sobral and Cross Valley–Wiman Formations. All diagrams show saturation below 0.3 T and dominance of low coercivity minerals (below 0.1 T) with unblocking temperatures close to 570℃ indicative of magnetite.